5-2020

Structural Aspects of Deformation Mechanism in Bulk Metallic Glasses and Deformation-induced Phase Transformation in Zirconium

Hui Wang
University of Tennessee

Recommended Citation

Wang, Hui, "Structural Aspects of Deformation Mechanism in Bulk Metallic Glasses and Deformation-induced Phase Transformation in Zirconium. " PhD diss., University of Tennessee, 2020.
https://trace.tennessee.edu/utk_graddiss/5887

To the Graduate Council:

I am submitting herewith a dissertation written by Hui Wang entitled "Structural Aspects of Deformation Mechanism in Bulk Metallic Glasses and Deformation-induced Phase Transformation in Zirconium." I have examined the final electronic copy of this dissertation for form and content and recommend that it be accepted in partial fulfillment of the requirements for the degree of Doctor of Philosophy, with a major in Materials Science and Engineering.

Wojciech Dmowski, Takeshi Egami, Major Professor

We have read this dissertation and recommend its acceptance:

Yanfei Gao, Hahn Choo, Steven Zinkle

Accepted for the Council:

Dixie L. Thompson

Vice Provost and Dean of the Graduate School

(Original signatures are on file with official student records.)

Structural Aspects of Deformation Mechanism in Bulk Metallic Glasses and Deformation-induced Phase Transformation in Zirconium

A Dissertation Presented for the
Doctor of Philosophy
Degree
University of Tennessee, Knoxville

Hui Wang
May 2020

Dedication

To my husband, my parents and my little sister, for their love and supporting.
To all my family and friends, for their help and company.

Acknowledgements

First of all, I would like to thank my adviser, Dr. Wojciech Dmowski, who led me not only to learn about metallic glasses but also to explore the research world. I always appreciated his step by step tutoring in experimental skills and data analysis, and his kind guide in the occasionally difficult life in a foreign country. Thanks for his elaborate guide and direction, great patience, and generous support as an advisor and friend. I also greatly thank my co-adviser, Dr. Takeshi Egami, who always presents me the big pictures of my research when I've been lost in the details. Thanks for his inspirational ideas, passion to the complex topics, and great attitude to research that will influence my future academic life. I would also express thanks to my committee members, Dr. Hahn Choo, Dr. Yanfei Gao, and Dr. Steven Zinkle, for their valuable time and instructions and the useful discussions.

This work could not be done without the help of the following great people in sample preparation, experiment setup and data analysis. I would like to express my gratitude to Dr. Yoshihiko Yokoyama from Tohoku University, and Dr. Jittisa Ketkaew from Yale University, who generously provided the high-quality bulk metallic glass samples. I am also grateful to beamline staffs at Advanced Photon Source (APS), Argonne National Laboratory, including Dr. Jonathan Almer, Dr. ChihPin Chuang, and Dr. Jun-Sang Park at 1-ID, Dr. Douglas Robinson at 6-ID, Dr. Yang Ren at 11-ID. I would also like to thank Dr. Hongbin Bei who kindly gave me access to the cutting and testing machines in his lab and Mr. Doug Fielden in the MSE department machine shop who cut many nice samples for me. Specially, I would like to thank my previous colleague, Dr. Yang Tong, for the detailed instructions in experiment and data analysis and valuable discussions helping me better understand the complex mechanical properties in bulk metallic glasses. In addition, I want to thank my previous and current colleagues, Dr. Takuya

Iwashita, Dr. Chae Woo Ryu, Dr. Yuya Shinohara, Yadu Sarathchandran and Leo Zella for the useful discussions and help during the beamline experiments.

Finally, I would like to thank my husband, Zengquan Wang, for his help to conduct structural study in APS, for his extensive assistances to my research work, for his understanding, supporting and tender cares. Without him, I would not have this valuable abroad research experience and could not go this far as a graduate student. I would also like to thank my parents and little sister for their countless support and love.

Abstract

Bulk metallic glasses are promising structural materials due to some prominent mechanical properties, such as high strength. While, the limited RT plasticity is the Achilles' heel of BMGs that impedes their application. Therefore, the study of the room temperature (RT) plasticity of bulk metallic glasses (BMGs) is essential and challenging. Due to the intrinsic disordered structure, the "defects" in metallic glasses (MGs) are only qualitatively described. It's well established that "elastic" deformation of BMG is locally heterogeneous and non-affine because of the local topological rearrangement (LTR) which is related to the emerging shear transformation zones (STZs) that control the nature of the plastic deformation beyond yielding.

To understand the large compressive plasticity of Zr-based BMGs with high Zr atomic fraction and some noble-metal based alloys, the structure of BMGs during mechanical deformation should be investigated.

This dissertation addresses three critical issues related to the plastic behavior of metallic glasses and the α to ω phase transition of Zr during high pressure torsion (HPT):

1. Quantification of the deformation "defects" in metallic glasses. We have conducted in-situ high energy X-ray diffraction experiments and anisotropic pair distribution function (PDF) analysis to quantify the "defects" activated by external stresses in metallic glasses with a proposed strain ratio parameter, $\frac{\varepsilon_0}{\varepsilon_\infty}$. Our results based on this characterization method reveal the microscopic origin of plasticity in some metallic glasses.
2. Correlation of the microstructure to the plasticity of BMGs. Through the compression mechanical tests and literature review, we found that the proposed parameter is consistent with the plasticity measured for various BMGs and provides a method to predict the plasticity of BMGs. Since the parameter is obtained from the structure characterization

during deformation, the correlation between the parameter and the plasticity is well established.

3. Elucidation of the α to ω phase transition of HPT-Zr. Using the high energy X-ray diffraction and the Rietveld refinement, the structure change of the Zr with increasing shear strain under high-pressure torsion is investigated, including the phase fractions and texture evolution. Finally, the α to ω phase transformation pathway is clarified.

Table of Contents

List of Tables

List of Figures

Chapter 1 Introduction

Bulk metallic glasses (BMGs) are novel materials with the disordered structure in a metastable thermal state. These two features result in some distinct thermal and mechanical properties. BMGs are rapidly cooled from the liquid state avoiding crystallization and inherit the corresponding liquid structure. Therefore, the structure of BMG is macroscopically isotropic with a spatial variation of the local surrounding environment for each atom.

Comparing to conventional metals and alloys, BMGs stand out for their extraordinary mechanical properties, such as the ultrahigh yield strength and elastic limit (~2%) [1, 2]. In addition, BMGs' wear, corrosion, and oxidation resistances are also high [3]. These make BMG a promising candidate as structural materials. However, the very limited room temperature (RT) plasticity hinders their engineering application. Most BMGs don't show much of a tensile plasticity and will fracture almost right away above yield strength, whereas they behave better under compression where limited plasticity is exhibited. However, BMGs with some plasticity can become brittle after annealing at the temperature below the glass transition temperature, T_g. The described plastic behaviors imply complex deformation mechanism of BMGs. In addition, the deformation "defects" of BMGs are unobservable and not well-defined. This further inhibits the investigation of the deformation mechanism of BMGs. The first part of this work mainly focuses on the structure and the deformation mechanism of BMGs.

The Zr-based BMGs, especially BMGs with high Zr fraction, show large plasticity. Understanding the structural response to the external stimulus for the Zr-based BMG can help the study of the deformation mechanism of BMGs. We also study the structure evolution of crystalline Zr under shear strain. We find that the phase transition of α to ω phase in Zr is still unclear.

Therefore, the α to ω phase transition and the texture evolution is explored in the second part of this work.

The development of the BMGs, the fabrication, mechanical properties, the corresponding applications, the structure and the mechanical deformation are first reviewed in Chapter 2. Then, more details related to the room temperature (RT) plastic deformation are introduced in 2.2. Section 2.3 introduces the structure of the α, β, and ω phases of the crystalline Zr, the reported phase transitions between them, and the texture evolution during mechanical processing by rolling.

Chapter 3 presents the experimental setups of the in-situ high energy X-ray diffraction and methodology of diffraction data analysis (anisotropic pair distribution function) to obtain structural information for BMGs.

To understand BMGs' plastic deformation and its correlation with the structure, deformation "defects" should be quantified. In Chapter 4, the method to quantify deformation "defects" is established through the measurement of the local strain relaxation. We proposed the strain ratio parameter, $\frac{\varepsilon_0}{\varepsilon_\infty}$. Then we examined the effect of the thermal history of BMGs on their strain ratio parameters. Furthermore, the strain ratio parameters for various BMGs, such as Zr-based, Pd-based, La-based and Pt-based etc. are investigated. Comparing the strain ratio parameter with the plastic behavior of these BMGs, the ability of the strain ratio parameter for plasticity characterization is verified, and the correlation of the microstructure with the plasticity of BMGs is established.

The second part of this dissertation, Chapter 5, discusses the α to ω phase transformation pathway and the texture evolution of pure Zr during high pressure torsion (HPT) process. Through high energy X-ray diffraction and the Rietveld refinement, the structural change of the α to ω phase induced by shear strain is quantified. Moreover, the texture evolution with shear strain is elucidated through the pole figures (PFs). Finally, the α to ω phase transformation pathway is obtained.

The primary goal of this work is to correlate the macroscopic plasticity to the microscopic structure deformation of BMGs under elastic deformation. Another goal is to clarify the α to ω phase transition of the HPT-Zr. These two goals are achieved by my research work as described in this dissertation. Conclusions and questions in the course of this work are addressed in the Chapter 6.

Chapter 2 Literature review

2.1 Introduction of BMGs

2.1.1 The fabrication of BMGs

The first metallic glass, $Au_{75}Si_{25}$, was unintentionally produced by Duwez et. al. in 1959 [4, 5 4, 5]. Through the so-called splat-quenching of the Au-Si liquid with the cooling rate of about 10^6 °C/s, this first metallic glass was made into irregular thin film with thickness varying from 1 to 20 μm. About 15 years later, Chen [6] reported the "double roller" rapid quenching method with the cooling rate of about 10^5 °C/s to form the more uniform thin ribbon metallic glass with thickness up to 100 μm. Then, by quenching the melted metallic liquid sealed in the capillary into water, Chen [7] synthesized the ternary Pd-Si-Cu BMG rods with diameter of 1 to 3 mm at a significantly lower cooling rate, about 10^3 °C/s. In 1984, Kuai et. al. [8] formed the Pd-Cu-Si and Pt-based BMGs with diameter above 1 cm using the boron oxide fluxing method. Then, in order to prepare large and uniform MGs, researchers started to develop compositions that can be easily vitrified rather than investigating rapid quenching techniques only. Even though the proposed glass forming ability (GFA) rules are empirical, today's BMGs of different alloy systems can be vitrified through the simple metal mold casting method with much lower cooling rate, under 100 $℃/s$ [9, 10]. This great progress in sample preparation propelled the study of MG substantially because of the accessibility of the uniform MG samples with large size.

The fabrication of MGs has been improved significantly. In addition to the preparation of experimental samples, more and more commercial BMG products can be massively manufactured. The melt spinning technique realizes the batch production of soft magnetic Fe-based MG ribbons that are widely used as the high-efficiency transformer cores. The thermoplastic forming (TPF) accomplishes the mass production of BMG products with complex shapes [11]. The Liquid Metal company use the melting-injection-molding method to manufacture BMG products for various uses [12].

2.1.2 The properties and applications of BMGs

BMGs have some distinct mechanical properties because of their disordered atomic arrangements. BMGs exhibit super high strength and hardness, much higher than their crystalline counterparts (Fig. 2.1) [13]. The $Co_{43}Fe_{20}Ta_{5.5}B_{31.5}$ BMG, for example, was reported to have ultrahigh fracture strength of 5,185 MPa [14]. The absence of “defects”, such as dislocation in crystalline materials, contributes to the super high strength of BMGs which almost reaches the theoretical limit. Also, the elastic limit of BMGs is very high, about 2%, indicating the ability of elastic energy storage of BMGs. This high elastic limit enables BMGs’ application in many sporting goods, such as golf club and tennis racket frame (Fig. 2.2). Because of the high strength, high hardness and self-sharpening, BMG are used as warhead of the armour-piercing fin-stabilized discarding sabot (Fig. 2.2). In addition, BMGs show excellent wear and corrosion resistance [15, 16] resulting in the application of MG coating on tools like knife edge (Fig. 2.2). Next, BMGs present good irradiation resistance [17] due to the intrinsic disordered structure. The bulk modulus of MGs is about 6% smaller than the crystalline materials with similar composition [18] and the shear modulus of MGs is significantly smaller, ~30%, than the corresponding crystalline material [18, 19, 20]. The above outstanding mechanical properties make BMG a promising structural material. However, MGs also bear some disadvantages, such as the lack of work hardening and limited room temperature plasticity, which prevents the industrial application of BMGs.

In addition, some features of BMGs remarkably facilitate their fabrication. BMGs exhibit good net shape formability at relatively low temperature [11]. In contrast to most conventional metals and alloys that are usually cast at very high temperatures, above the melting temperature T_m, MGs

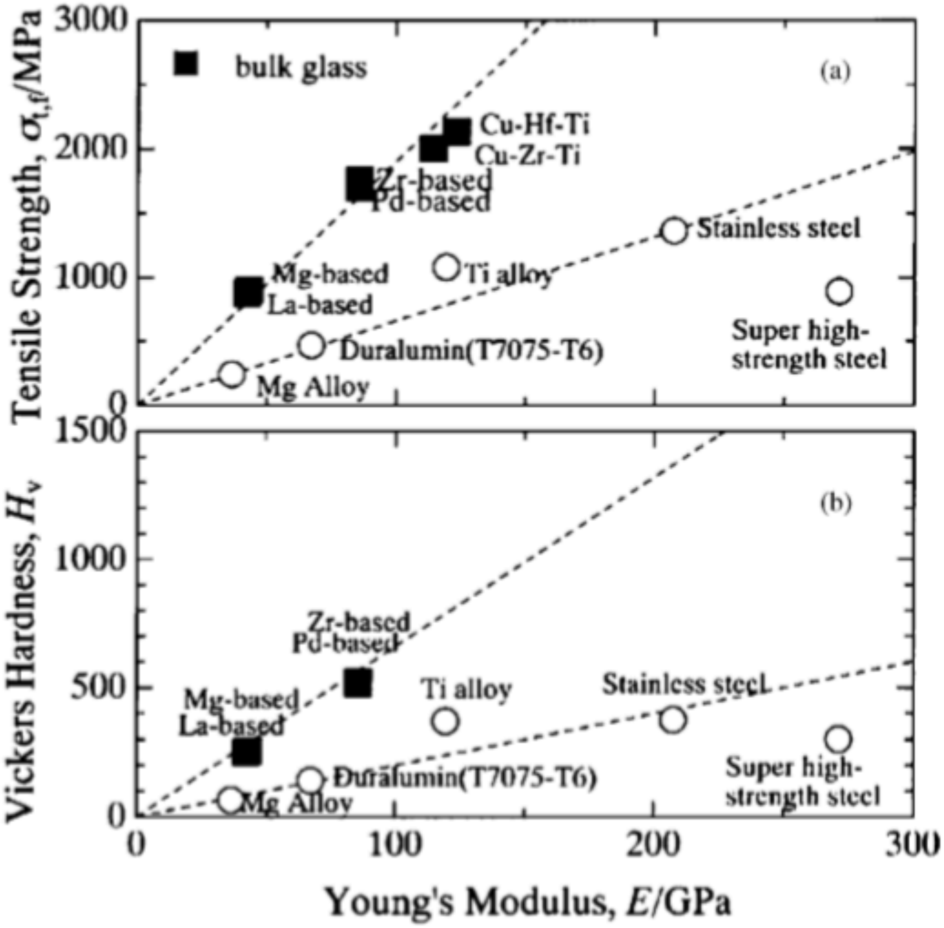

Figure 2.1 The dependence of Vickers Hardness and tensile strength on Young's modulus for various metallic glasses (Copyright (2002) by The Japan Institute of Metals.)

Figure 2.2 Applications of MGs.

can be fabricated at the temperature far below T_m owing to the stable undercooled liquid state of MGs above T_g. Unlike crystalline materials, the volume of MGs doesn't change that much during cooling. This avoids the formation of porosity of MGs during processing. Moreover, the surface of the MGs after fabrication is much smoother eliminating the necessity of the second process like polishing. This processing advantage leads to the application of MGs as parts with high precision and surface requirements [11].

Some MGs also present some other intriguing properties. For instance, Fe, Co, Ni-based MGs show notable soft magnetic properties resulting in the use of BMGs as transformer iron core (Fig. 2.2) to greatly decrease the energy loss, and it is already widely used [21]. NASA developed metallic glass gears (Fig. 2.2) utilized in a robot investigating the surface of Europa where the operating temperature is below -170 °C.

2.1.3 The structure of BMGs

BMGs are amorphous materials without long-range translational and rotation symmetry. This structural disorder is clearly demonstrated from the X-ray diffraction (Fig. 2.3). Unlike the thin and bright rings indicating the sharp Bragg peaks for polycrystalline powder material (Fig. 2.3(a)), the two-dimensional (2D) XRD pattern of BMGs shows some broad and dispersive rings (Fig. 2.3(b)). Despite the structural disordering, BMGs present short-range structural topological and chemical order. Therefore, BMGs are homogeneous and isotropic macroscopically; while, locally exhibit statistical distribution of short-range ordering [22]. The atomic-level elastic modulus, especially the shear modulus, have a spatial variation [23] because of distribution of local atomic environment. Defects, deviation from the periodic lattice, are important structural feature of conventional crystalline metallic alloys. However, it’s hard to define and observe the structural “defects” in BMGs (Fig. 2.4), since the local atomic environment has a distribution without distinguishable boundaries. Due to the variation of the local atomic environment, some atoms tend to be easier to move than others when subjected to external stresses. The more mobile atoms can be defined as activated “defects” of BMGs. And to define the “defect”, a cut-off in the continuous distribution of some structural parameter needs to be set.

Theories and models to investigate the crystalline structure are already well-developed. Additionally, various techniques and methods to study and characterize the structure of crystalline materials are mature, such as SEM and TEM. However, for disordered BMGs without obvious structural “defects”, these microstructure characterization techniques are not effective which further inhibits the investigation of BMGs. Now, there are only limited experimental techniques such as high-energy X-ray diffraction and neutron scattering [24, 25], or advanced TEM techniques, and computer-based modeling, such as MD simulation [26] to explore the structure of BMGs.

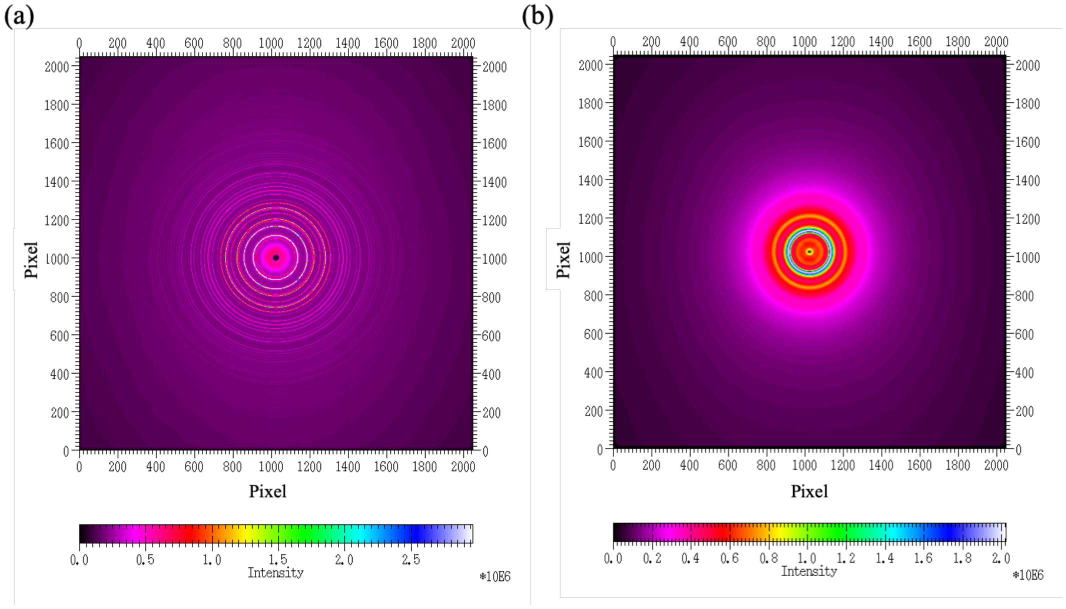

Figure 2.3 2-D XRD pattern of (a) MgO and (b) $Mg_{66}Zn_{30}Ca_4$ BMG.

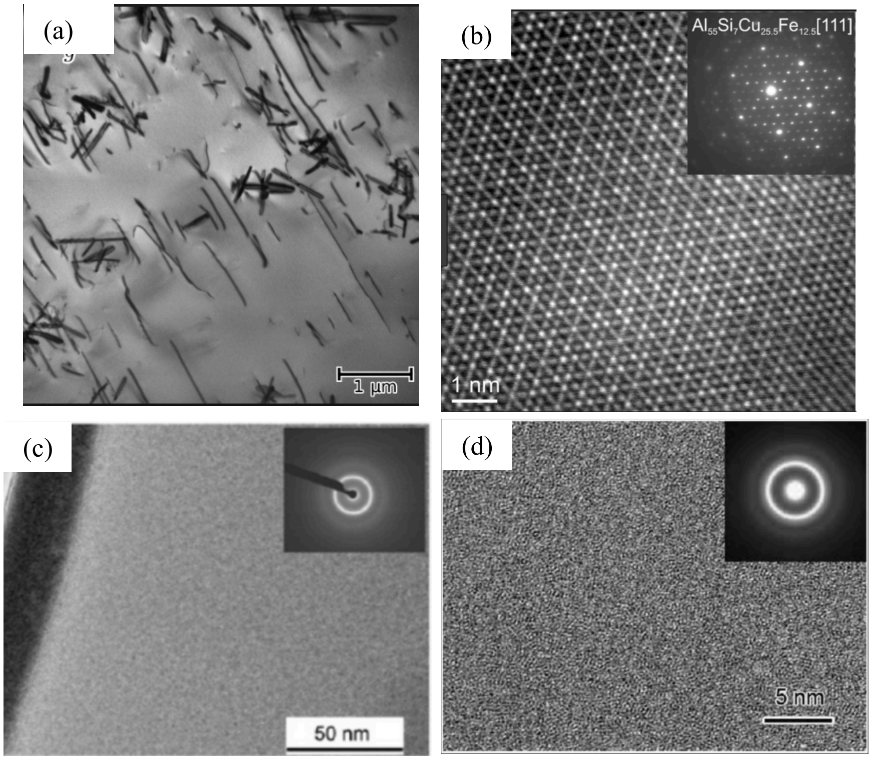

Figure 2.4 TEM pattern of (a) crystalline material and (b) BMG.

2.1.4 The mechanical deformation of BMGs

The mechanical deformation of BMGs seems simpler than that of the conventional metallic alloys since the elastic deformation is followed by the limited plastic deformation without work hardening. However, after taking a closer look, we're surprised by the complexity of the mechanical deformation of BMGs.

BMGs are usually assumed to be elastically isotropic and follow the Hook's law at the macroscopic level. However, the statistical distribution of the local structure, as mentioned in section 2.1.3, leads to the heterogeneity of elastic deformation in BMGs [27]. When subjected to elastic stresses, part of atoms in BMGs deform elastically whereas the other sites, about 25%, deform anelastically [27]. The 25% sites under anelastic deformation are the fertile spots activated by the external stresses. The local plastic strains are accommodated through the anelastic deformation.

The plastic deformation of BMGs is also complicated. As shown in the deformation map in Fig. 2.5, the plastic deformation of BMGs varies with temperature, stress, and strain rate [28]. At the high temperature and low strain rate/stress, the deformation of BMGs is homogeneous macroscopically. At the low temperature or high strain rate/stress, BMGs deform inhomogeneously where the plastic deformation is mainly localized in the shear band (SB). During the homogeneous deformation, when the shear stress linearly changes with the strain rate, BMGs behave as a Newtonian fluid which normally happens above T_g. While, if the change of the shear stress with the strain rate is nonlinear, BMGs are more viscous and behave as the Non-Newtonian fluid.

At RT, BMGs undergo the inhomogeneous deformation when the stresses imposed on the specimen is beyond the yield strength. The plastic deformation is localized in the thin shear band which initiates immediately after yielding. The shear band has the important practical influence on

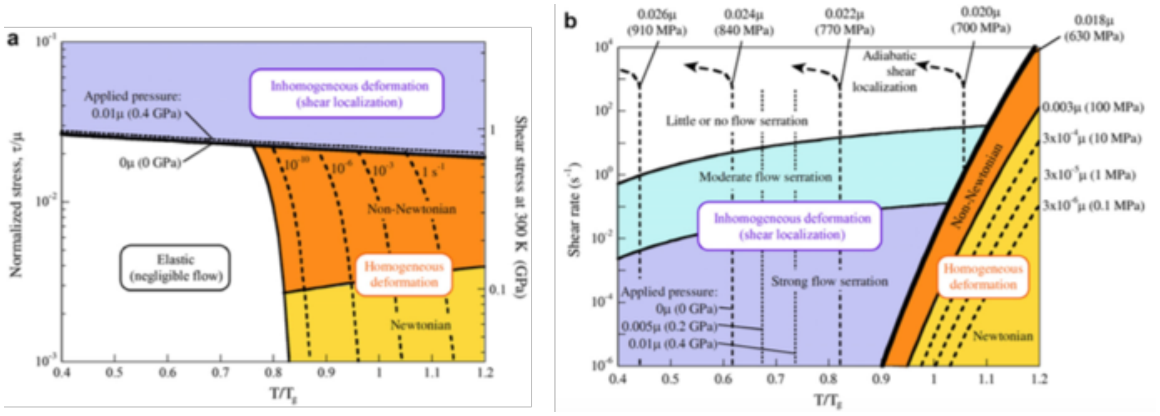

Figure 2.5 Deformation maps of BMGs [14].

the yielding, plasticity, toughness and eventually the utility of MGs. Most MGs fail because of the formation of the dominant shear band. SB forms through the percolation of some locally perturbed regions - STZ [29, 30] where the atoms show higher mobility under loading. The thickness of the shear band is about 10-100 nm [31, 32, 33, 34, 35]. The structure in the SB is rejuvenated and more disordered [36, 37]. Also, there is a temperature surge in the SB [38] for about 650-1200K [39, 40]. The nanovoids are observed in SB under tensile state [41, 42]; while, sometimes the nanocrystallization occurs in SB under compressive stress state [41, 43]. Fracture occurs when the propagation of SB is not prevented and, consequently, the plastic strain accumulates in the one, dominant SB. Therefore, without any constraints to the SB propagation, MGs fail in a brittle way.

2.1.5 The deformation mechanisms of BMGs

The deformation mechanism of BMGs is elusive due to the disordered structure and the limited experimental techniques. It’s essential to clarify the deformation mechanism which directly influences the mechanical properties of BMGs. And the elucidation of the deformation mechanism of BMGs can help to establish the correlation of the mechanical deformation to the microstructure of BMGs. Several deformation models are proposed to understand the plastic deformation of MGs. Among them, two models are widely used, free volume model proposed by Spaepen [44] and shear transformation zone (STZ) model by Argon [45].

Cohen and Turnbull [46] found a strong correlation between molecular diffusion and free volume in liquids and glasses and proposed the free volume model. Later, Spaepen [44] applied this free volume model to the deformation of MGs. In this model, the plastic deformation of BMGs is accommodated by several local diffusive-like jumps of single atom (Fig. 2.6). To accomplish this jump, a vacancy – about 80% of the average atomic volume based on the hard sphere model – near the jumping atom is required. The free volume is the difference of the atomic

volume after jump. The thermally activated jump occurs in all directions, so the atoms jumping back and forth result in the formation and annihilation of the free volume which keeps an equilibrium state. Only when some stresses are applied, jumps to one direction win over and the plastic deformation is accommodated through the formation of free volume.

The free volume model explains some mechanical behavior of MGs, such as the boundary between the homogeneous and inhomogeneous deformation. Also, the annihilation of the free volume can describe the density increase and the embrittlement of the BMG after annealing. However, even though the free volume model successfully explains some phenomena of MGs, the basic assumption of the free volume model is still controversial. The volume of the “vacancy” which is about 80% of the average atom volume is too large for MGs which turns out to be only 10% [47]. Moreover, the much small density change of the BMG after annealing [48, 49] leading to the ductile to brittle transition also questions the free volume model.

Inspired by the deformation of disordered bubble raft model under shear stress [50], Argon proposed the shear transformation zone model to describe the mechanism of plastic deformation

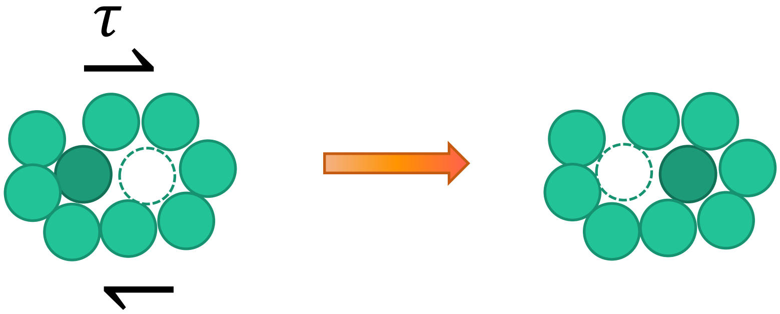

Figure 2.6 Schematic illustration of free volume [44].

of MGs below T_g [45]. In the shear transformation theory, Argon [45, 51, 52] pointed out that the shear transformation initiates around the free volume sites, known as shear transformation zone which includes 4-6 atoms (Fig. 2.7). The atom rearrangement in STZ produces local shear strain. When small stress is applied these STZs are surrounded by the undeformed elastic atomic matrix. With the increasing of the external stress, more STZs are activated around the free volume site which results in the contiguity of the shear transformation. The contiguous STZs removes the elastic surroundings and leads to the plastic deformation of MGs. The STZ model explain the plastic deformation of MGs at low temperature, high temperature (still below T_g) and during the steady state flow stage. Several parameters, such as flow stress, of Pd-based BMGs predicted by STZ model are in good accordance with that from experiment which verifies the STZ model.

According to STZ model, the free volume is much smaller and reasonable. It can well explain the anelastic and plastic deformation, the formation and propagation of shear band [45, 51, 52]. Later on, this model has been widely used to study MGs. Also, a lot of efforts have been made to improve this model. One of the essential research topics is the size of the STZ. After the investigation with different techniques and simulations, the reported STZ size shows a large

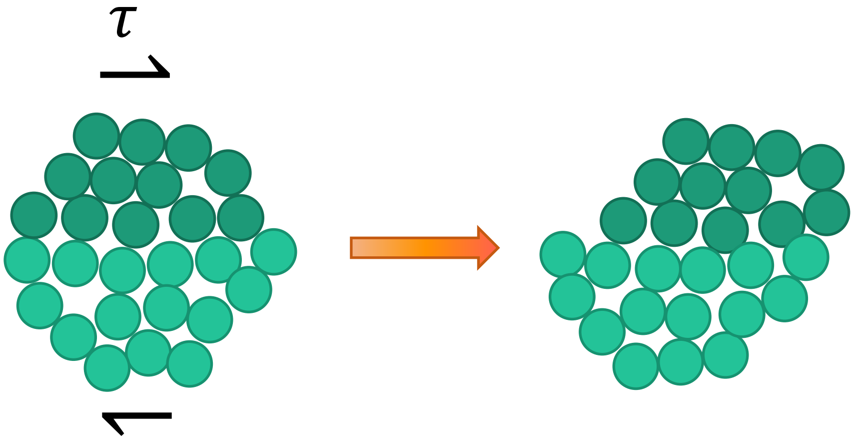

Figure 2.7 Schematic illustration of STZ [45].

variation from 5 atoms to hundreds [53, 54, 55, 56]. The study of the thermal activation process of MG through activation-relaxation technique shows that the trigger of STZ is accomplished by the rearrangement of five atoms and the size of the triggered STZ is small, below 10 atoms [53]. It also suggests that the ambiguity of STZ sizes results from the investigation of different deformation stages of MGs. The STZ size based on the plastic deformation analysis is very large, about hundreds of atoms, owing to the rapid growing and overlapping of STZs [56]. While, the size of STZ is small from the study of the elastic deformation where STZ is still isolated [54].

Because the deformation of MGs is emergent, there is no way to map the STZ distribution until now.

2.2 The room temperature plastic deformation of BMGs

The RT plastic behavior of BMGs is complicated as discussed before. First, most BMGs are usually brittle materials with a small plastic strain. Secondly, there is an asymmetry in plastic behavior of BMGs in compression and tension tests. The plasticity of BMGs subjected to tension is much smaller than that under compression. The loading modes significantly affect the fracture processes of BMGs [57, 58, 59, 60, 61]. Most BMGs, such as Zr-based, Pd-based, and Cu-based, present some plasticity with compressive stresses, whereas under tension, they break immediately upon yielding. This is because the tensile normal stress facilitates local dilation which is introduced through the formation of the shear band. Subsequently, voids are developed, and the shear band is unconfined under this condition. This is verified by the typical fracture feature of BMGs under tension, the flat cores which is the aggregation of voids surrounded by the vein-like pattern (Fig. 4 in ref [57]). Furthermore, the significant deviation of the angle between the fracture surface and the loading direction from 45º [57, 62] also illustrates the fracture of BMGs under tension is in both shear mode and normal mode resulting in the tension-induced brittleness of BMGs. In contrast, fracture of BMGs under compression is a pure shear mode with the vein-like pattern (Fig. 3 in ref [57]) and the fracture angle close to 45º [57]. Lastly, BMGs with some plasticity undergo ductile-to-brittle transition after annealing (Fig. 2.8).

2.2.1 Characterization of plastic behavior in BMGs

There is no standard way to characterize the plasticity BMGs. Until now, mechanical tests for crystalline materials are utilized to measure the plasticity of BMGs. But the standard mechanical test methods for crystalline materials may not be suitable to BMGs. Even if we assume that standard methods are also applicable to BMGs, the sample dimension requirements of the standard methods are too large to meet due to the limited size of BMGs. It's still difficult to develop the standard mechanical tests for BMGs and classify their plastic in an unambiguous manner.

Most BMGs are brittle and show little plasticity under tension, thus, their plasticity cannot be measured through tension tests. In addition, large sample is required for the tension tests which

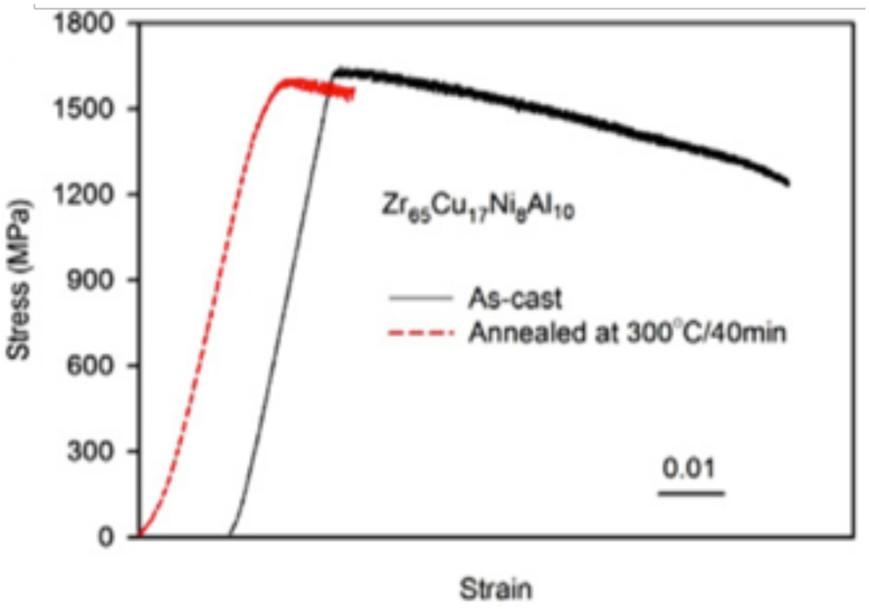

Figure 2.8 Stress-strain curve of Zr-based BMG [63].

excludes BMGs without good GFA. Therefore, tension test is not an ideal way to measure and compare the plasticity of various BMGs.

On the contrary, the exhibition of the compressive plasticity and the accessibility of much smaller sample dimension make the compression mechanical test a more suitable method to measure the plasticity of BMGs. But still close attention should be paid to sample size when conducting the compression test. When the ratio of the sample height to diameter/width, h/d, is smaller than 1, the formation and propagation of the shear band are restricted geometrically [64] which can artificially enhance the overall plasticity of BMGs. Therefore, the h/d of the compression specimen should be larger than 2. In addition, the subtle imperfections in the specimen geometry, such as miscut and deviations from orthogonality, can affect the compression response [65]. Because under uniaxial compression the tilting or bending of the non-orthogonal specimen leads to the geometrical confinement of the shear band and artificial plasticity.

Fracture toughness, by definition, is the energy combining the energy of the newly created surfaces with the energy dissipated in the plastic process zone through plastic deformation [66] which is related both to the strength and the plasticity. According to dimensional requirements of standard ASTME399, the size of the standard sample for the fracture toughness measurement are way too large for BMGs. Therefore, "non-standard" size samples are typically used and conditional toughness, K_Q, instead of K_c, is measured for BMGs. However, the fracture toughness of BMG varies significantly with the sample geometry [67]. Chen and his colleagues [66] found a way to measure the fracture toughness of BMGs which considerably reduces the scatter of the fracture toughness, for example, the fracture toughness for $Zr_{44}Ti_{11}Cu_{10}Ni_{10}Be_{25}$ BMG is 109 MPa$\sqrt{m} \pm 3$ MPa$\sqrt{m}$. In their fracture toughness measurement, BMG samples (Fig. 2.9Figure 2.9) used are with flawless notch surface fabricated via TPF.

In this work the assessing of the plasticity is achieved using the fracture toughness for the single $Zr_{44}Ti_{11}Cu_{10}Ni_{10}Be_{25}$ BMGs and the compression mechanical test for other BMGs with different compositions.

2.2.2 Intrinsic factors influencing the plasticity of BMGs

There are two essential intrinsic factors that influence the plasticity of BMGs: the composition and the thermal history of the BMG. The plasticity of BMGs is very sensitive to their compositions. BMGs with some noble elements, such as Pt, show unusually large plasticity [68], whereas other BMGs, such as La-based and Ce-based, are very brittle with almost no plasticity [69]. Moreover, for BMGs synthesized with the same elements but different atomic fractions, the plasticity varies a lot [70]. Even some minor tuning of the composition can dramatically change the plasticity of BMGs.

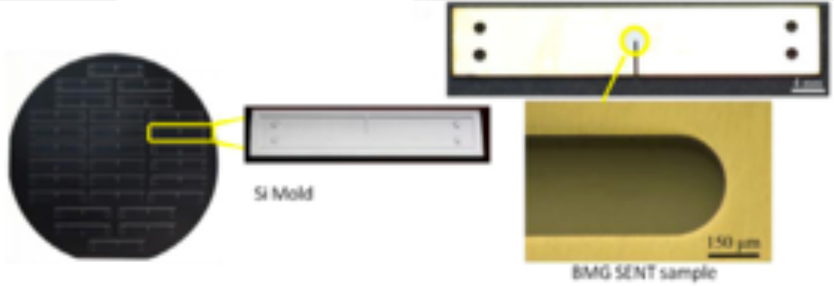

Figure 2.9 BMG samples to measure the fracture toughness [66].

The thermal history has significant influence on the mechanical behavior of the BMGs [71, 72]. BMGs are rapidly cooled from the liquid state thus the structure of BMGs is inherited from the supercooled liquid. The structure of the undercooled liquid depends on the temperature. Therefore, the fictive temperature, T_f, corresponding to the undercooled liquid state from which the glass is frozen, is used to characterize the thermal history of BMGs [73]. The effects of T_f on the structure and mechanical properties of some BMGs have been studied [71, 72]. Since the mobility of atoms in the undercooled liquid increases with the raising temperature, the BMG with higher T_f, have more disordered structure [74] and the ability to accommodate more plastic strains. This is confirmed by the study of Kumar et al [75] where they found the increase of the bending strain to failure and the decrease of the G/B with increasing T_f/T_g in Pt-based, Zr-based and Pd-based BMGs (as shown in Fig. 2.10).

2.2.3 Improvement of the RT plasticity of BMGs

Besides the two intrinsic factors mentioned above, there are some extrinsic factors that affect the RT plasticity of BMGs by confining the shear band propagation. Accordingly, various methods are reported to improve the plasticity of BMGs.

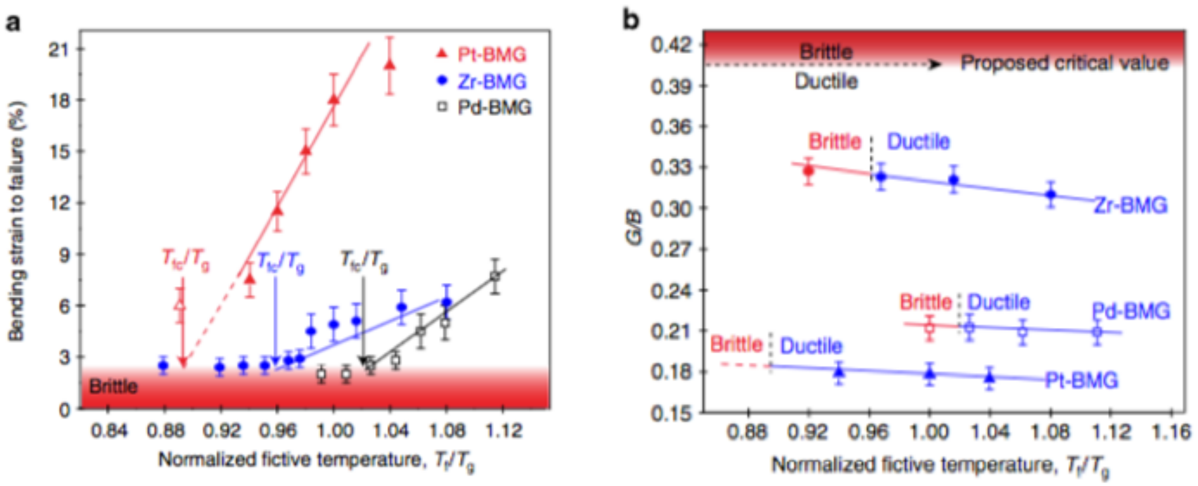

Figure 2.10 Effect of fictive temperature on (a) critical strain and (b) elastic constants [75].

The composition tuning is attempted to increase the plasticity of BMGs [76, 77]. Based on the investigation of the effect of a specific element on the plasticity of some BMGs, the establishment of the correlation of the composition to the plastic behavior of BMGs is tried as well. Another efficient way to improve the plasticity is to change the thermal history, specifically, by increasing the fictive temperature of BMGs through the rejuvenation of BMGs, such as thermo-mechanical creep [67, 72] and severe plastic deformation, i.e. cold rolling [78], shot peening [79], and high-pressure torsion [80]. Recent study proposed that cryogenic cycling [81] also induces the structural rejuvenation of BMGs. Additionally, several approaches are proposed to confine shear bands in BMGs to improve the plasticity. Significant reducing of the specimen size can suppress the formation of shear bands in MG [82, 83]. Machining specimen into some specific shapes, such as notch with remarkably small h/d, hinder the propagation of the shear band [84, 85, 86]. Introducing obstacles, such as crystal precipitates, by fabrication of BMG composites [79, 87] can also suppress the shear band propagation.

Among all the methods above, the thermo-mechanical creep is the most effective way so far. Composition tuning only works for a few of BMGs and the empirical rules are still illusive. Severe plastic deformation introduces microscopic defects, such as cracks and ruptures that sometimes embrittle MGs. Meanwhile, not all BMGs can endure severe plastic deformation. The thermo-mechanical creep works for all kinds of BMGs. Moreover, it can continuously tune the structure of BMG by controlling creep parameters, such as creep temperature, stress and time [76]. Also, it eliminates the risk of damaging BMG samples since the applied creep stress is below the yield strength. The last but not the least, it retains the amorphous structure of BMGs.

BMG composites is a good idea to balance the strength and plasticity. However, so far, the control of the size, fraction and the distribution of the crystalline precipitates is difficult. And the way to toughen the interface between the MG and the crystalline needs further investigation. If these problems are solved, BMG composites could become a promising material for the industrial application.

2.3 The phase transitions and texture evolutions in crystalline Zirconium

2.3.1 Phase diagram of Zr

As shown in the P-T phase diagram in Fig. 2.11, under different temperature and pressure, Zr forms three different phases: α, β, and ω [88]. The α phase with hcp structure is stable under ambient conditions. The β phase with bcc structure is a high temperature/pressure phase which cannot be observed at the ambient conditions due to the reverse transformation to α phase during cooling or unloading. The ω phase with the simple hexagonal structure is metastable at ambient conditions. At ambient pressure, the α phase will transform to β phase at about 1100 K; The boundary between α phase and ω phase is ambiguous where the transformation pressure of the α

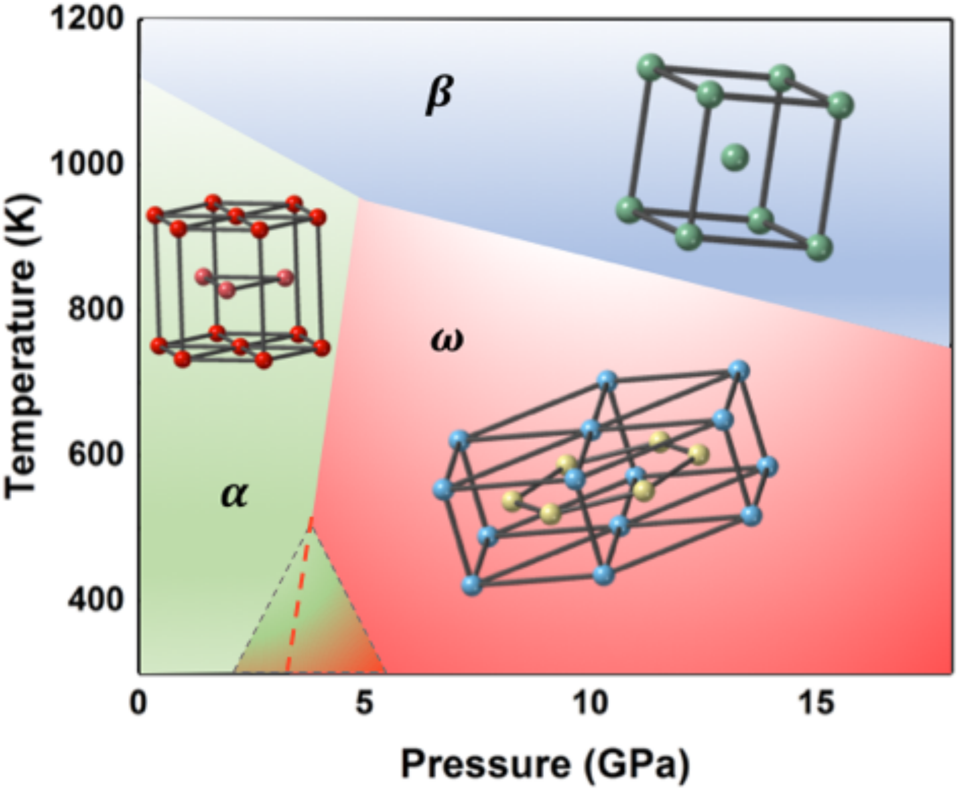

Figure 2.11 P-T phase diagram of Zr.

to ω phase varies from 2.3 to 6 GPa at room temperature (RT) [89, 90]. The uncertainty of the α to ω phase boundary is caused by the shear-induced phase transition which will be discussed later (section 2.3.3). The ω to β phase boundary as shown in Fig. 2.11 indicates that there is a phase transition from ω to β when the pressure is large enough [89, 90].

2.3.2 Phase transitions in Zr

The phase transitions of group IV transition metals (Ti, Zr, and Hf) share some similarities: hcp transforms to bcc at high temperature and to simple hexagonal at high pressure, and simple hexagonal transforms to bcc at high temperature/pressure [91]. The phase transition between α and β is diffusive transformation [90, 92]. The β phase transforms to α phase through a shuffle of every second (110) plane by $\frac{1}{6}[1\bar{1}0]$ combined with a contraction in the [001] direction and an extension in the $[1\bar{1}0]$direction. In this way, the (110) planes of the β phase become the close packed planes, (0001), of the α phase (Fig. 2.12) [90]. The orientation relationship of transition between α and β is clearly shown in Fig. 2.12.

The transition between ω and β phase is martensitic [91, 93]. The β to ω phases transition, as shown in Fig. 2.13, is accomplished through the collapsing two out of every three of (111) planes towards each other in the [111] direction transforming the (111) plane of the β phase to the (0001) plane of the ω phase [91]. The OR of this transformation is also obviously shown in Fig. 2.13.

In contrast to the explicit phase transition of α ↔ β phases and ω ↔ β phases, there is still debate about the mechanism of the α to ω transformation. The dispute is mainly over the participance of the β phase in the α to ω phase transition. The Silcock [94] proposed a direct martensitic transformation from α to ω which is supported by recent experimental study with advanced method, such as neutron diffraction and synchrotron. The OR for the direct transition

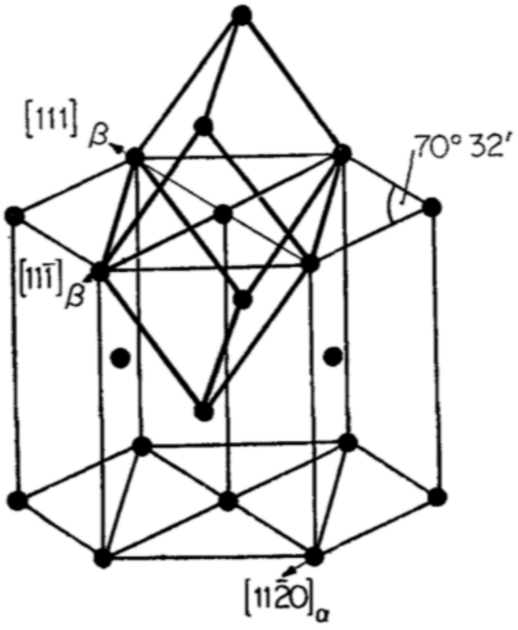

Figure 2.12 Phase transition between α and β [95].

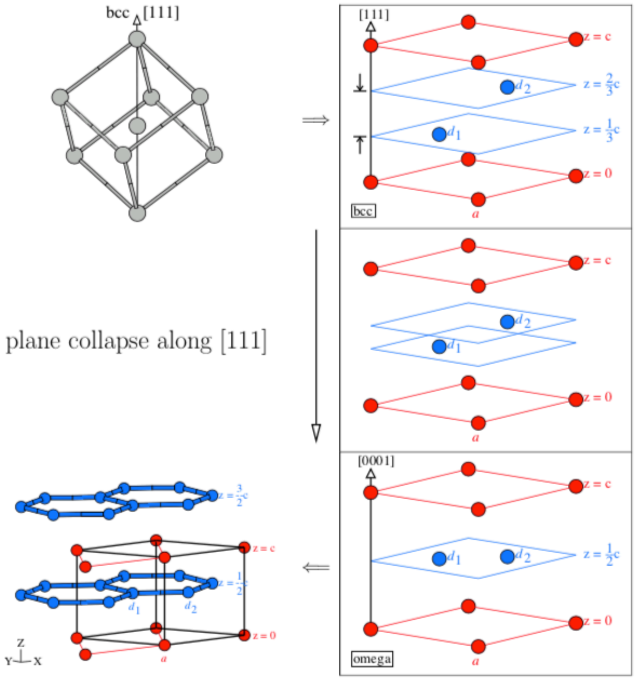

Figure 2.13 Phase transition between β and ω [96].

is $(0002)_{\alpha} \parallel (11\bar{2}0)_{\omega}$, $[11\bar{2}0]_{\alpha} \parallel [0002]_{\omega}$. While, Usikov and Zilbershtein [97] suggested an indirect transition through the intermediate β phase. The corresponding OR obtained through TEM studies was $\{0002\}_{\alpha} \parallel \{01\bar{1}1\}_{\omega}$, $<10\bar{1}0>_{\alpha} \parallel <\bar{2}\bar{1}31>_{\omega}$. Alternative pathway was also suggested for Ti by Trinkle et al. [98] from ab-initio calculations with OR $\{0002\}_{\alpha} \parallel \{0\bar{1}11\}_{\omega}$, $<11\bar{2}0>_{\alpha} \parallel <01\bar{1}1>_{\omega}$. There are other studies [99, 100, 101] on the pathway and OR of the indirect α to ω phase transition in Zr and Ti, whereas no unanimous conclusion is drawn on this problem.

2.3.3 HPT studies and texture in Zr

The shear induced α to ω phase transition under low pressure ~ 2.3 GPa in zirconium was first observed by Zilbershtein et al. [102] in 1975. Recently, there have been more reports on this transition by using HPT [89, 103, 104]. Shear strain contributes to the α to ω phase transition and decreases the pressure initiating the phase transition. Therefore, the ambiguity of α to ω phase boundary of Zr is caused by different shear strains introduced through different mechanical tests.

During HPT process, torsion texture is introduced which severely influences the investigation of the mechanism of the phase transition. Min Ma et al. reported the textures of hot-rolled Zr and the cold rolled Zr [105]; however, the texture evolution due to HPT deformation has not been established. Moreover, HPT can refine microstructure [89] where nano-grained omega phase was fabricated after HPT.

Chapter 3 Experimental Setup and Data Analysis

3.1 Introduction

Metallic glasses have short-range order and moderate middle-range order. The structure information about the short-range order contained in the PDF, pair distribution function g(r), is obtained by Fourier transformation of the structure function S(Q) determined from diffuse x-ray scattering experiments .

The local topological rearrangements (LTRs) – bond cutting and reforming - activated by the imposed external stresses are the sites of STZs. LTR is an emergent event and disappears when the sample is unloaded. The classical crystalline structure characterization techniques, such as TEM and High Resolution TEM, are not applicable to characterize LTR which appears as the response of BMGs to the external stress. This is due to the ambiguous boundaries between the "defects" and their surroundings and the fast activation process of LTRs which requires high time resolution. Therefore, PDF is a suitable technique to characterize the deformation "defects" of BMGs by acquiring the structural information of BMGs before and during deformation where the difference between them corresponds to the "defects" activation.

The diffraction pattern of crystalline Zr is complicated owing to the severe overlapping of the Bragg peaks of α, β, and ω phase. Particularly almost all the Bragg peaks of β and ω phase are overlapped. To study the HPT induced phase transition and differentiate Bragg peaks of each phase, high-energy X-ray diffraction is conducted as an advantageous technique in light of its high spatial resolution.

3.2 Experimental details

The high-energy X-ray diffractions were conducted at ID-1, ID-6, and ID-11 beamlines of the Advanced Photon Source (APS), Argonne National Laboratory. As shown in Fig. 3.1, electrons

Figure 3.1 Advanced Photon Source.

are accelerated in a linear accelerator first, then injected into the booster synchrotron and finally injected into the storage ring. The monochromatic high-energy high-brightness X-ray suitable for our research is generated by the acceleration of electrons travelling in the storage ring, then formed by optical components in the front end, and finally obtained in the beamline hutch. For the purpose of our in-situ X-ray diffraction experiment, beamline ID-6 offers furnace, ID-11 offers mechanical testing system (MTS), and ID-1 offers both furnace and MTS. The detailed introduction to each beamline can be found at https://www.aps.anl.gov/Beamlines.

The in-situ high-energy x-ray diffraction setup is shown in Fig. 3.2. The diffraction data are collected when BMG sample is subjected to different compressive stresses. The energy of the X-ray beam is about 100 keV. The beam size is usually 0.2× 0.2 mm which may be subtly adjusted according to the specific sample conditions. 2-D detectors with 2048 × 2048 pixels and 200 µm × 200 µm pixel size are used to collect data. The 2-D detector is placed ~390 mm behind the sample.

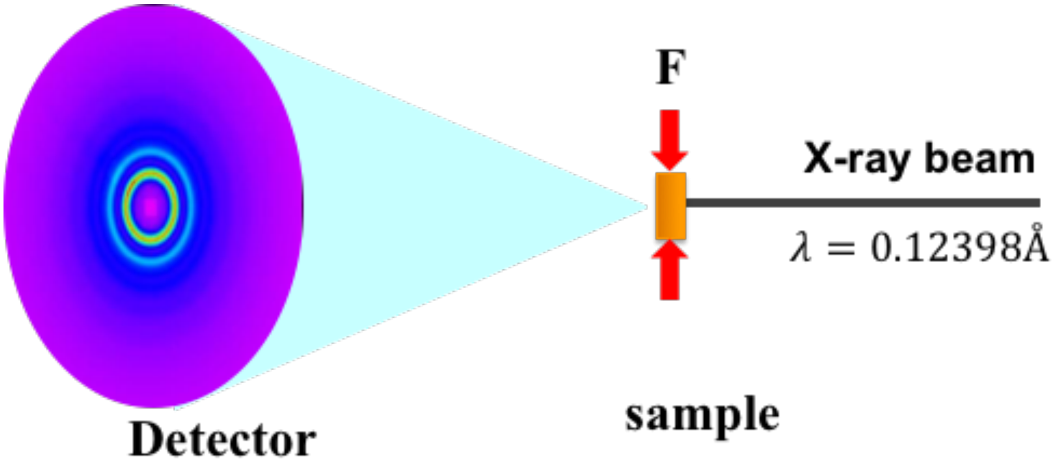

Figure 3.2 In-situ high-energy x-ray diffraction.

Calibration is performed using the CeO2 NIST powder standard.

Given the transmission diffraction geometry, the background and absorption correction are critical issues. Thus, the specific specimen size, especially the thickness directly affecting the absorption, for high energy X-ray diffraction study is required. For in-situ compression or tension structural study, rectangular/cylindrical specimens with thickness/diameter about 1mm are used. For some heavy absorption samples, such as the Pt-based BMG, the thickness should be even less, < 0.5 mm. For ex-situ structural study, thin slice samples with 0.5mm thickness are prepared. In order to obtain good statistical results, appropriate exposure time and the number of frames has to be optimized for every sample with the constraint of saturation intensity for a 2-D detector. In addition, dark images are also collected to reduce the signal from thermal excitation in 2-D detector and noise in the electronics.

To study the phase transition and texture of HPT-Zr, the ex-situ high-energy X-ray diffraction is performed with Zr samples sitting on the goniometer, as shown in Fig. 3.3. For this study, PDF

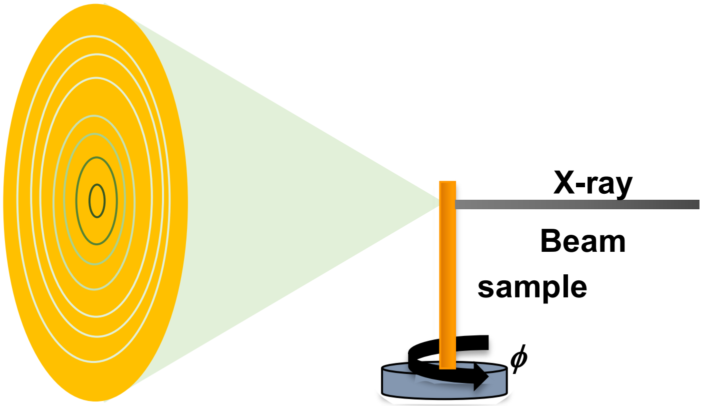

Figure 3.3 Schematic diagram of the high energy x-ray diffraction with a goniometer and a 2D detector.

is not needed. So, to acquire a higher Q-space resolution, 2-D detectors are placed further, ~120 cm, behind the sample.

3.3 Data analysis

The sample scattering amplitude from the high energy X-ray diffraction is:

$$\Psi(\vec{Q}) = \frac{1}{\langle b \rangle} \sum_{\upsilon} b_{\upsilon}(Q) e^{i\vec{Q}\cdot\overrightarrow{R_{\nu}}}$$

where $\vec{Q}$ is the diffraction vector, $b_{\upsilon}(Q)$ is the scattering factor of υth atom, $\overrightarrow{R_{\nu}}$ is the position of υth atom. The problem is that this $\Psi(\vec{Q})$ cannot be directly measured. Only the intensity of the diffracted beam, which is directly related to the square of the magnitude of $\Psi(\vec{Q})$, that is, $|\Psi(\vec{Q})|^2$ can be acquired from diffraction experiment. And all coherent scattering is given as

$$\frac{d\sigma_c}{d\Omega} = \frac{1}{N} \sum_{\nu,u} b_{\nu} b_u e^{i\vec{Q}\cdot(\overrightarrow{R_{\nu}}-\overrightarrow{R_u})}$$

where $\frac{d\sigma_c}{d\Omega}$ is coherent scattering cross-section, N is the number of atoms in a system. Total scattering structure function or structure function is

$$S(\vec{Q}) = \frac{\frac{d\sigma_c(\vec{Q})}{d\Omega} + \langle b \rangle^2 - \langle b^2 \rangle}{\langle b \rangle^2}$$

where the term $\langle b \rangle^2 - \langle b^2 \rangle$ is named Laue monotonic scattering.

In addition to the scattering by the sample, the diffraction data collected during experiment also includes the scattering from the background, such as air and experimental apparatus, and some noises, such as the dark current from the detector. Therefore, to get clean structure signal from samples, first, the data from the instrumental background should be collected and subtracted from the total scattering data; then several corrections should be done [106]. Second, absorption correction due to that some part of scattering is absorbed by sample itself is needed. Third, multiple scattering correction, such as multiple scattering of photons in a sample before arriving to the detector, should be applied. Forth, the Compton scattering, and fluorescence has to be removed. Fifth, proper normalization is required to obtain structure function. Any errors in corrections have significant effects on the final structure function. But all these complex procedures can be done easily using PDFgetX2 or PDFgetX3 software. Details about these corrections can be found in the manual of PDFgetX.

PDF is obtained from the structure function through the Fourier transformation

$$g(r) = \frac{1}{2\pi^2 \rho_0 r} \int_0^\infty [S(Q) - 1] \sin(Qr) Q dQ$$

where ρ_0 is the atomic density. There are some other forms of PDFs, such as reduced PDF (G(r)), pair density function ($\rho(r)$), and radial distribution function (R(r))

$$G(r) = 4\pi\rho_0 r[g(r) - 1]$$

$$\rho(r) = \rho_0 g(r)$$

$$R(r) = 4\pi\rho_0 r^2 g(r)$$

The coordination number can be calculated from R(r) by

$$N_c = \int_{r_1}^{r_2} R(r)dr$$

For a material with known coordination numbers, R(r) also acts as a benchmark to evaluate the processing procedure of structure function.

The above data analysis process works perfectly for isotropic materials. BMGs with anisotropic structure (e.g. BMGs under uniaxial stress), however, need another approach to data analysis, such as anisotropic PDF analysis including spherical harmonics expansion and Bessel transformation. First, the spherical harmonics expansion is applied to get the isotropic and anisotropic structure functions.

$$S(\vec{Q}) = \sum\nolimits_{\ell,m} S_\ell^m(Q) Y_\ell^m(\frac{\vec{Q}}{Q})$$

where $Y_l^m\left(\frac{\vec{Q}}{Q}\right)$ is the spherical harmonics. Then, the Bessel transformation is applied to get the corresponding PDF.

$$g(\vec{r}) = \sum\nolimits_{\ell,m} g_\ell^m(r) Y_\ell^m(\frac{\vec{Q}}{Q})$$

$$\rho_\ell^m(r) = \frac{i^\ell}{2\pi^2}\int_0^\infty S_\ell^m(Q) J_\ell(Qr) Q^2 dQ$$

where $J_\ell(Qr)$ is a spherical Bessel function. Based on the symmetry of the sample, the odd order terms are eliminated. Because the structural information of higher order terms is negligible, only the 0th and 2nd order terms are often used. The isotropic PDF, g_0^0, is a measure of the volume strain. The anisotropic PDF, g_2^0, is a measure of the r-dependent strain, ε(r), and the structural anisotropy. The mechanical deformation of BMGs is investigated by examining the change of these two components of the total PDF induced by external stimulus.

Chapter 4 Correlation of local topological rearrangement and plasticity of BMGs

4.1 Introduction

The study of the room temperature (RT) plasticity of bulk metallic glasses (BMGs) is essential since the RT plasticity is Achilles' heel of BMGs that limits their application. Unlike crystalline materials with well-defined defects, such as dislocations, the “defect” of BMG is obscure [107] due to the intrinsic disordered structure of BMGs. This structural disorder hinders the study of BMGs, especially their deformation mechanism, and makes the traditional structural characterization methods, such as SEM and TEM, not applicable. To explore the deformation mechanism of BMGs, several theoretical models are proposed to define the deformation defect of BMGs. Among these models two are widely used, the free volume model by Spaepen [44] and the shear transformation zone (STZ) by Argon [45]. Based on these two models, researchers are trying to find the correlation between plastic behavior of MGs and intrinsic properties of STZ. Different STZ sizes of ~200-700 atoms [56], ~100 atoms [55], ~25 atoms [54], and 5 atoms [53] are reported through the molecular simulation and nanoindentation techniques. It is suggested that larger volume of STZs contributes to the higher plasticity [56]. But no unanimous agreement has been reached on the size of STZ. Moreover, the STZ density is not determined in BMGs.

From the macroscopic perspective, at room temperature the plastic deformation of BMGs is determined by the formation and propagation of shear bands. The RT plastic deformation is localized in the thin shear bands. The formation and propagation of the dominant shear band without any confinements leads to the brittle fracture of BMGs. The formation and interaction of the multiple shear bands make the BMG behave in a ductile way exhibiting large plasticity before fracture.

It is proposed that the plastic deformation and fracture of BMGs is a competition between the normal and the shear stress driving deformation. Thus, the plasticity correlates to the ratio of shear modulus to bulk modulus, G/B, directly relating to the Poisson's ratio [74, 108]. After the investigation of several BMGs, it's suggested that BMG with large Poisson's ratio tends to show more plasticity. However, with more BMGs tested, it turns out that the Poisson's ratio only works well for limited number of BMGs with similar chemistry and fails to characterize the plasticity for quite a few BMGs.

In this section, through the in-situ high energy X-ray diffraction of BMG samples under elastic deformation, the effect of "defects" in BMGs are quantified by the strain ratio parameter from the microscopic structure perspective for the first time. Furthermore, correlation of the microscopic deformation to the macroscopic plasticity is established.

4.2 Experiments

Amorphous $Zr_{44}Ti_{11}Cu_{10}Ni_{10}Be_{25}$ was obtained from Materion. Then high temperature annealing was conducted to manipulate the fictive temperature, T_f. The "notch" fracture toughness was measured by a collaborating team from Yale University [109]. The other BMG samples in this work are prepared through arc melting and copper mold casting into rods and slabs of different sizes. Samples with different dimensions are cut by electrical discharge machine (EDM) for the in-situ diffraction. Stresses below the yield strength of each BMG are applied on the compression cell where the sample sits between anvils. Considering the X-ray absorption, the thickness of BMG samples should be small, at least less than 1 mm, for the transmission diffraction geometry. The setup of the in-situ high-energy X-ray diffraction is shown in Fig. 3.2. The diffraction is carried out on each sample under elastic deformation at beamline 1-ID of the Advanced Photon Source

(APS), Argonne National Laboratory. The diffraction data are collected for BMG under different stresses, from 0 MPa to 1200 MPa every 200 MPa for Zr-based, Pd-based BMGs and Pt-based, and from 0 MPa to 700 MPa every 100 MPa for La-based, Ce-based and Mg-based BMGs. The beam energy is 100 keV ($\lambda = 0.12358$ Å). 2-D detector with 2048 × 2048 pixels and 200 μm × 200 μm pixel size is used. The 2-D detector is placed ~390 mm behind the sample. Calibration is performed using the CeO2 NIST powder standard. The in-situ high-energy x-ray 2D diffraction data are processed by FIT2D software [110] for the preliminary corrections.

Compression test is conducted on some BMGs. Because of the different glass forming abilities of these BMGs, the compression samples are not exactly with the same dimension. But the ratio of the width to height are similar (Table 4.1). Moreover, to ensure that no shear bands is confined by the anvils during the compression tests, the shear bands are checked through the optical microscope (OM). This excludes the false plasticity.

4.3 Anisotropic PDF analysis

The local anisotropic behavior of BMG under elastic deformation is experimentally observed [27]. The elliptical 2D diffraction pattern from BMGs subjected to uniaxial stresses directly reveals the structural anisotropy of BMGs (Fig. 1 in ref [111]). The anisotropic PDF analysis is applied to analyze the anisotropic diffraction data. First, the spherical harmonic expansion is used to extract the isotropic and anisotropic structure functions, $S_0^0(Q)$ and $S_2^0(Q)$. Then, through Bessel transformation, the isotropic and anisotropic pair distribution functions, $g_0^0(r)$ and $g_2^0(r)$, are obtained from the isotropic and anisotropic structure functions, respectively (more details in Section 3.3 and ref [111]). The isotropic component of the PDF, g_0^0, is a measure of the volume strain. The anisotropic component, g_2^0, quantifies the r-dependent strain, $\varepsilon(\mathrm{r})$ (equation 4.2), and

Table 4.1 Sample dimensions of BMG samples for compression.

Sample	Size (mm)
Pd30Ni50P20	$1.5 \times 1.56 \times 4.58$
Pd32Ni16Cu32P20	$0.69 \times 1.36 \times 3.63$
Pd38Ni14Cu28P20	$\phi 1.81 \times 4.08$
Pd40Ni40Si5P15	$\phi 1.96 \times 4.19$
Pd42.5Ni7.5Cu30P20	$\phi 1.98 \times 4.5$
Pd43Cu27Ni10P20	$1.41 \times 1.91 \times 4.59$
Pd44Ni12Cu24P20	$\phi 1.88 \times 4.66$
Pd50Ni34P16	$1.47 \times 1.49 \times 4.06$
Pd50Ni10Cu20P20	$\phi 2.26 \times 4.18$
Pd56Ni8Cu16P20	$\phi 0.89 \times 1.48$
Pd62Ni6Cu12P20	$\phi 0.91 \times 1.58$

the structural anisotropy when the BMG is subjected to stresses. To measure ε(r) and the anisotropy, a reference state of sample under affine deformation is introduced. The affine deformation is the linear transformation and a rigid body translation of atoms where the strain tensor for each atom in the system is uniform. The corresponding affine anisotropic PDF, $\rho_{2,aff}^{0}(r)$, is:

$$\rho_0 g_{2,affine}^{0}(r) = \varepsilon_{affine}\frac{2(1+\nu)}{3\sqrt{5}} r \frac{d}{dr}\rho_0 g_0^0(r) \qquad \text{Eq. 4.1}$$

Here the ρ_0 is the number density of the BMG, ν is the Poisson's ratio, ε_{affine} is the affine strain.

Then fit of the $\rho_{2,exp}^{0}(r)$ (equal to $\rho_0 g_{0,exp}^{0}(r)$) to the $\rho_{2,aff}^{0}(r)$ (Fig. 4.1 (a)) is performed. As shown in Fig. 4.1 (a), the fitting with unique strain works well at the long *r* range (~7-20 Å) reflecting that the strain beyond the first/second shell is equal to the average strain, or affine strain. However, at the low *r* range, especially in the first shell, the $\rho_{2,exp}^{0}(r)$ deviates from the $\rho_{2,aff}^{0}(r)$, which indicates the non-affine local deformation of these BMG samples under the macroscopic 'elastic' deformation. This deviation is the common structural response to the elastic deformation of all the BMG samples we measured. Compared to the $\rho_{2,aff}^{0}(r)$, the smaller amplitude of the $\rho_{2,exp}^{0}(r)$ in the first shell reveals that the local strain is smaller than the average strain leading to the conclusion that there is a local strain relaxation under stress.

4.4 Strain ratio parameter

In order to quantify the local strain relaxation, the strain ratio parameter, $\frac{\varepsilon_0}{\varepsilon_\infty}$, is proposed. The denominator, ε_∞, is the long-range average strain obtained from the fitting of eq.4.1 in the long *r* range. The numerator, ε_0, is the local strain, $\varepsilon_0 = \frac{\varepsilon_1+\varepsilon_2}{2}$. The ε_1 and ε_2 are the r-dependent strain,

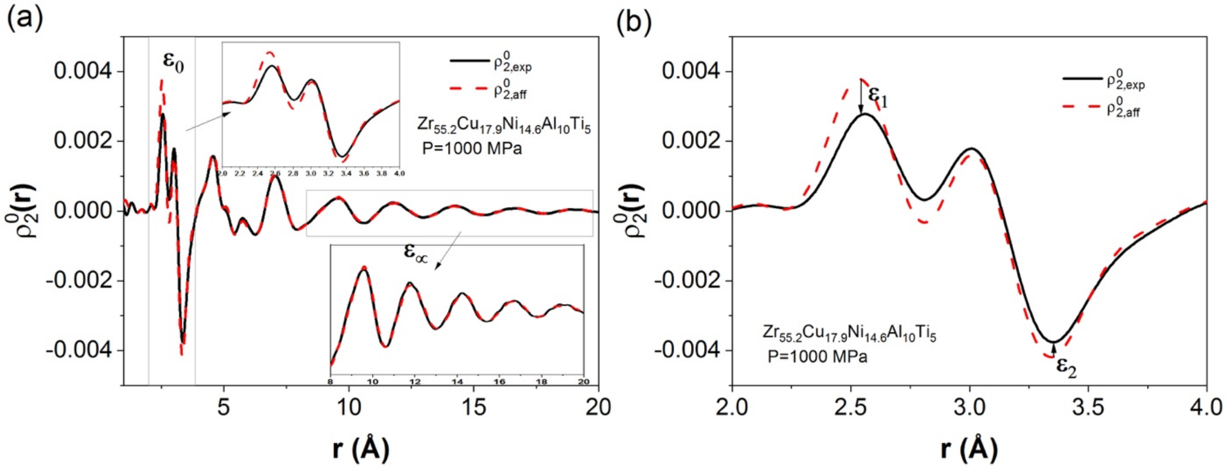

Figure 4.1 (a) The fitting of the experimental anisotropic PDF with the affine anisotropic PDF. (b) local r-dependent strain.

$\varepsilon(r_1)$ and $\varepsilon(r_2)$, determined by fitting in the range of first PDF peak, as shown in Fig. 4.1 (b). The *r*-dependent strain, $\varepsilon(r)$, is fitted through below equation,

$$\rho_0 g^0_{2,exp}(r) = \varepsilon(r)\frac{2(1+\nu)}{3\sqrt{5}}\, r\,\frac{d}{dr}\,\rho_0 g^0_0(r) \qquad \text{Eq. 4.2}$$

When BMG sample is subjected to some stresses, the local topological rearrangement (LTR) – bond cutting and reforming – is initiated to accommodate the strains, subsequently, leading to the local strain relaxation. This local strain relaxation is a common response to the deformation of BMGs which is shown by change of the *r*-dependent strains with *r* in Fig. 9 in ref [111] where the local strain is always smaller than the average strain. The strain ratio parameter, $\frac{\varepsilon_0}{\varepsilon_\infty}$, measuring the relaxed local strains, can quantify the amount of LTRs manifesting the intrinsic ability of the BMG to accommodate the strains during deformation. Therefore, this parameter, $\frac{\varepsilon_0}{\varepsilon_\infty}$, can indicate the plasticity of BMGs. Given the definition of $\frac{\varepsilon_0}{\varepsilon_\infty}$, the conjecture can be made that smaller $\frac{\varepsilon_0}{\varepsilon_\infty}$

indicates that glass capability to relax local strains is larger and resulting in larger plasticity of the BMG and vice versa.

The change of $\frac{\varepsilon_0}{\varepsilon_\infty}$ with stress exerted on the specimen is displayed in Fig. 4.2. The strain ratio parameter is constant for BMGs subjected to different stresses suggesting that the comparison of $\frac{\varepsilon_0}{\varepsilon_\infty}$ measured at different stresses is reasonable. This indicates the strain ratio parameter is an intrinsic parameter characterizing the glass ability of strain accommodation that won't change with the external stresses.

4.5 Correlation of LTR and plasticity of BMGs

4.5.1 Strain ratio parameters for BMGs with different thermal histories

The structure of the BMG is inherited from the liquid it's quenched from. Therefore, the thermal history has significant influence on the mechanical behavior of the BMGs. The cooling rate directly affects the thermal history of the BMG [75]. Annealing [49] and thermal-mechanical creep [67, 72] can tune the thermal history of the BMG to the more relaxed or rejuvenated state. Fig. 4.3 displays the strain ratio parameter for Zr-based and Pd-based BMGs with different thermal histories. The thermal history of these BMGs is modified through annealing, thermal-mechanical creep and cooling rate. The red bar represents the more rejuvenated state and the blue bar represents the more relaxed state. It shows that compared to the rejuvenated one, the more relaxed BMG exhibits larger strain ratio parameter indicating the smaller plasticity. Rejuvenation introducing disordering to the structure of BMG results in the increase of the plasticity. While, relaxation weakening the disorder tendency leads to the decrease of the plasticity of BMGs. This trend is consistent with the previous presumption that small strain ratio parameter indicates large plasticity. Therefore, this strain ratio parameter, $\frac{\varepsilon_0}{\varepsilon_\infty}$, can correctly relate to the plasticity of BMGs

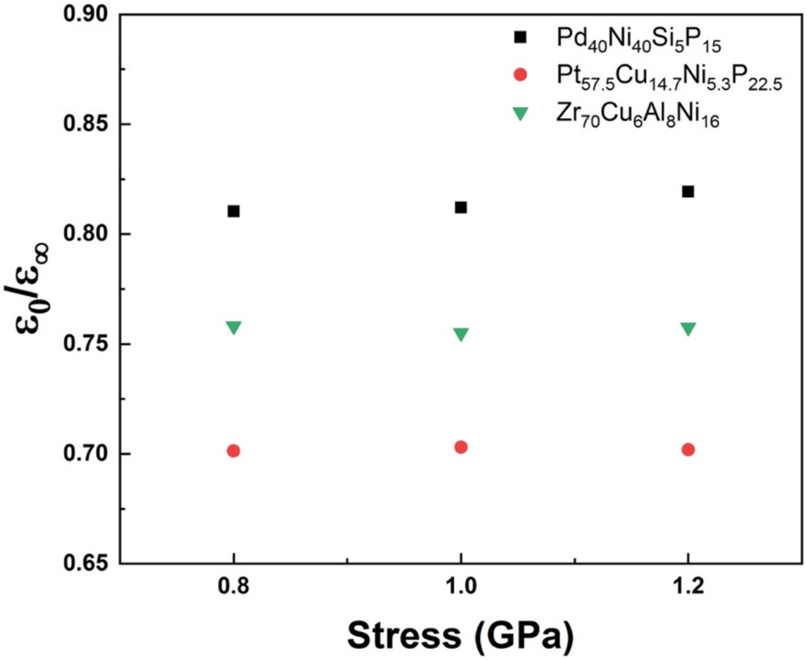

Figure 4.2 Strain ratio for BMGs subjected to different stresses.

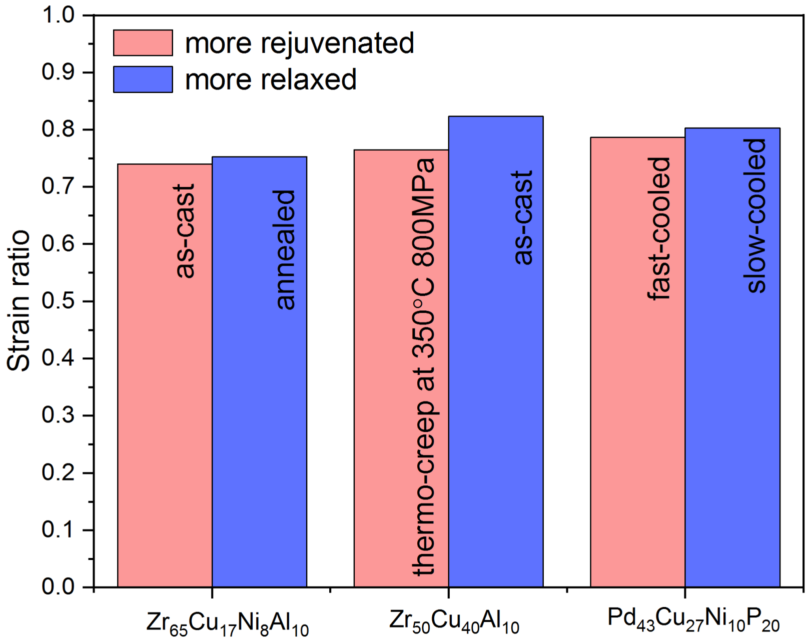

Figure 4.3 Strain ratio for BMGs of different conditions.

in different thermal state.

The thermal history of BMGs can be characterized by the fictive temperature, T_f, corresponding to the super-cooled liquid state from which the glass is frozen [73]. The effect of T_f on the structure and mechanical properties of BMGs has been studied [71, 72]. BMG with higher T_f has more disordered structure and exhibits larger plasticity. The fracture toughness, K_Q, for $Zr_{44}Ti_{11}Ni_{10}Cu_{10}Be_{25}$ increases with increasing fictive temperatures and saturates when T_f is above 390 ℃ [109]. The strain ratio parameters of these $Zr_{44}Ti_{11}Ni_{10}Cu_{10}Be_{25}$ BMGs are displayed in Fig. 4.4. The $\frac{\varepsilon_0}{\varepsilon_\infty}$ decreases with the increasing T_f and saturates when T_f reaches 390 ℃. Therefore, the $\frac{\varepsilon_0}{\varepsilon_\infty}$ is inversely proportional to the fracture toughness [109] of $Zr_{44}Ti_{11}Ni_{10}Cu_{10}Be_{25}$ BMG with different T_f which is consistent with the presumption in Section 4.4

4.5.2 Strain ratio parameters for Zr-based BMGs

The change of the strain ratio parameter, $\frac{\varepsilon_0}{\varepsilon_\infty}$, with the Zr atomic fraction of Zr-based BMGs is shown in Fig. 4.5 (a). The $\frac{\varepsilon_0}{\varepsilon_\infty}$ decreases with the increasing Zr atomic fraction indicating more plasticity for the Zr-rich BMGs. This trend is consistent with the results of the reported mechanical tests [112, 113, 114] that Zr-rich BMGs tend to show more plasticity. Based on the compression results [112, 113, 114], the Zr-based BMGs with $\frac{\varepsilon_0}{\varepsilon_\infty}$ below 0.77 exhibit ductility during deformation and show more plastic strains; while, when $\frac{\varepsilon_0}{\varepsilon_\infty}$ is above 0.77, the Zr-based BMGs is brittle and don’t show much plasticity or even breaks right away upon yielding. The compression mechanical tests are conducted on $Zr_{50}Cu_{40}Al_{10}$ and $Zr_{65}Cu_{17}Ni_8Al_{10}$ from the same rods used in the in-situ high energy X-ray diffraction sample. As shown in Fig. 4.5 (b), $Zr_{50}Cu_{40}Al_{10}$ shows very limited plasticity, whereas $Zr_{65}Cu_{17}Ni_8Al_{10}$ exhibits large plasticity. This is in line with the

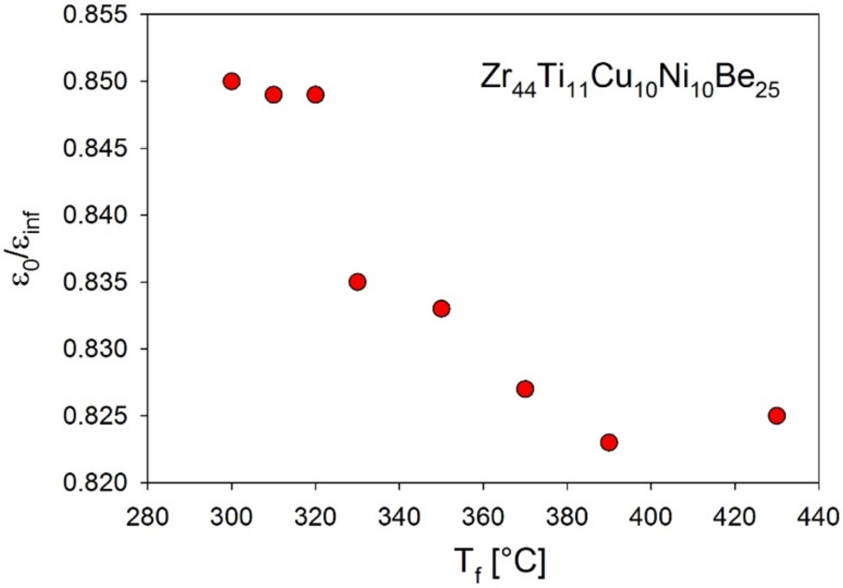

Figure 4.4 The strain ratio parameters of $Zr_{44}Ti_{11}Ni_{10}Cu_{10}Be_{25}$ with different T_f.

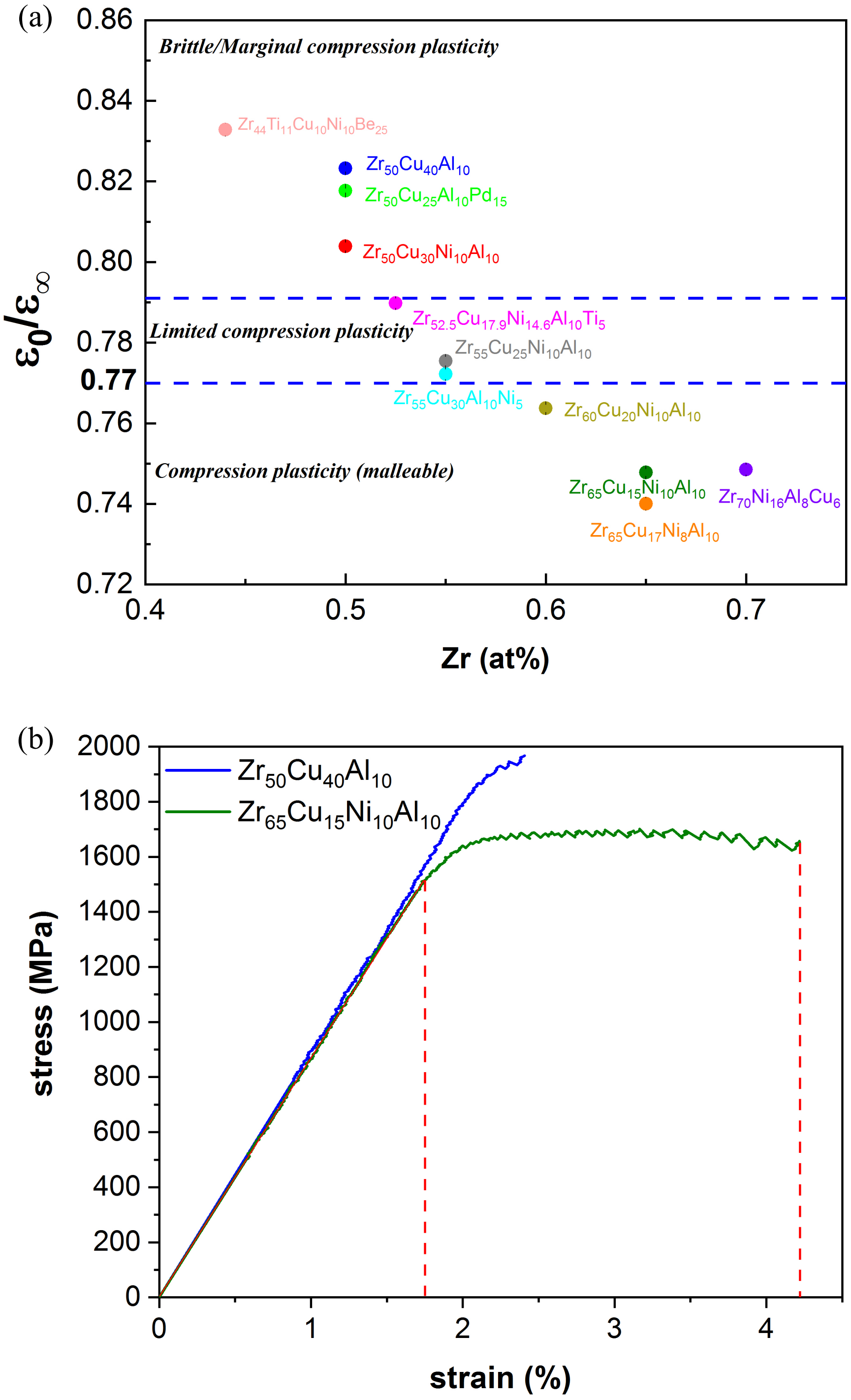

Figure 4.5 (a) The strain ratio parameters with error bars of Zr-based BMGs; (b) The stress-strain curves of Zr-based BMGs under compression.

strain ratio parameter and the brittle-to-ductile changeover at the critical value of 0.77.

4.5.3 Strain ratio parameters for Pd-based BMGs

The strain ratio parameters, $\frac{\varepsilon_0}{\varepsilon_\infty}$, for different Pd-based BMGs are displayed by circles with different colors in Fig. 4.6 (a). Fig. 4.6 (b) shows the stress-strain curves of the compression tests on some of these Pd-based BMGs with the same color as the circles in Fig. 4.6 (a). The $Pd_{42.5}Ni_{7.5}Cu_{30}P_{20}$ (pink one) without any plasticity has the largest $\frac{\varepsilon_0}{\varepsilon_\infty}$ among these BMGs in the compression tests. Above 0.77, with the decreasing of $\frac{\varepsilon_0}{\varepsilon_\infty}$, $Pd_{32}Ni_{16}Cu_{28}P_{20}$ (blue), $Pd_{38}Ni_{14}Cu_{28}P_{20}$ (green), and $Pd_{44}Ni_{12}Cu_{24}P_{20}$ (cyan) exhibit limited but larger plastic strains. The $\frac{\varepsilon_0}{\varepsilon_\infty}$ of $Pd_{50}Ni_{10}Cu_{20}P_{20}$, $Pd_{56}Ni_8Cu_{16}P_{20}$, and $Pd_{68}Ni_6Cu_{12}P_{20}$ decreases from 0.77 to 0.73. And the plasticity of these samples is relatively large and increasing (Fig. 4.6 (b)). The $Pd_{79}Ag_{3.5}P_6Si_{9.5}Ge_2$ has the noteworthy small $\frac{\varepsilon_0}{\varepsilon_\infty}$ which is 0.67. The compressive stress-strain curve of $Pd_{79}Ag_{3.5}P_6Si_{9.5}Ge_2$ is reported in [2] where the considerable plasticity is presented compliable with its smallest $\frac{\varepsilon_0}{\varepsilon_\infty}$ we measured. Therefore, Fig. 4.6 firmly verifies the conjecture made at the beginning that small strain ration parameter, $\frac{\varepsilon_0}{\varepsilon_\infty}$, indicates large plasticity. Moreover, the stress-strain curve suggests that the critical value of $\frac{\varepsilon_0}{\varepsilon_\infty}$ is 0.77 below which BMGs starts showing large plasticity.

4.5.4 Strain ratio parameters for other various BMGs

Strain ratio parameters for other BMGs with large Poisson's ratio, ν, are also measured (Fig. 4.7). It was suggested that with increasing ν BMGs present larger plasticity and tend to be ductile when ν is above 0.32 [108]. The Poisson's ratios of all the BMGs in Fig. 4.7 are above 0.32.

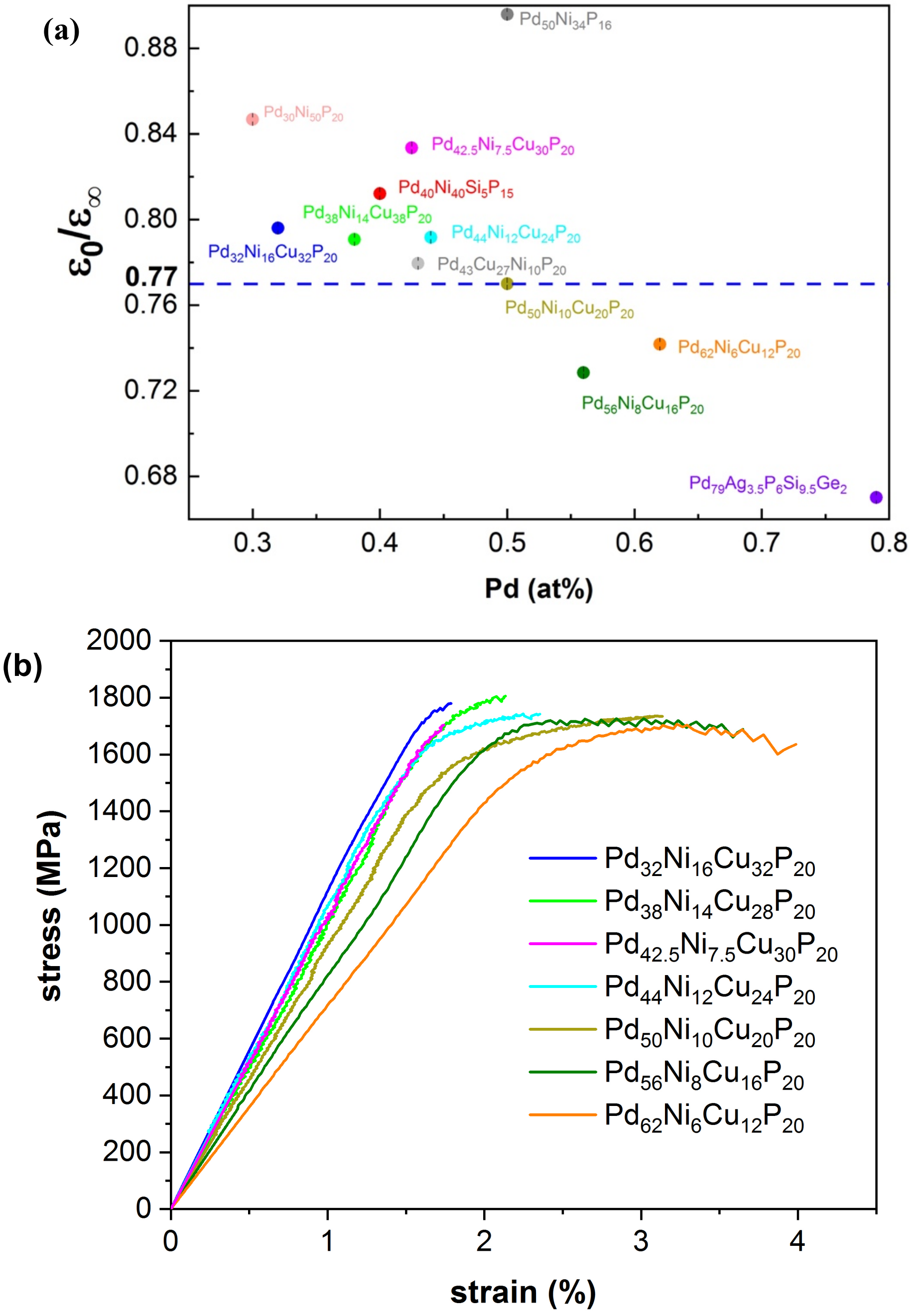

Figure 4.6 (a) The strain ratio parameters with error bars of Pd-based BMGs; (b) Compressive stress-strain curve of Pd-based BMGs.

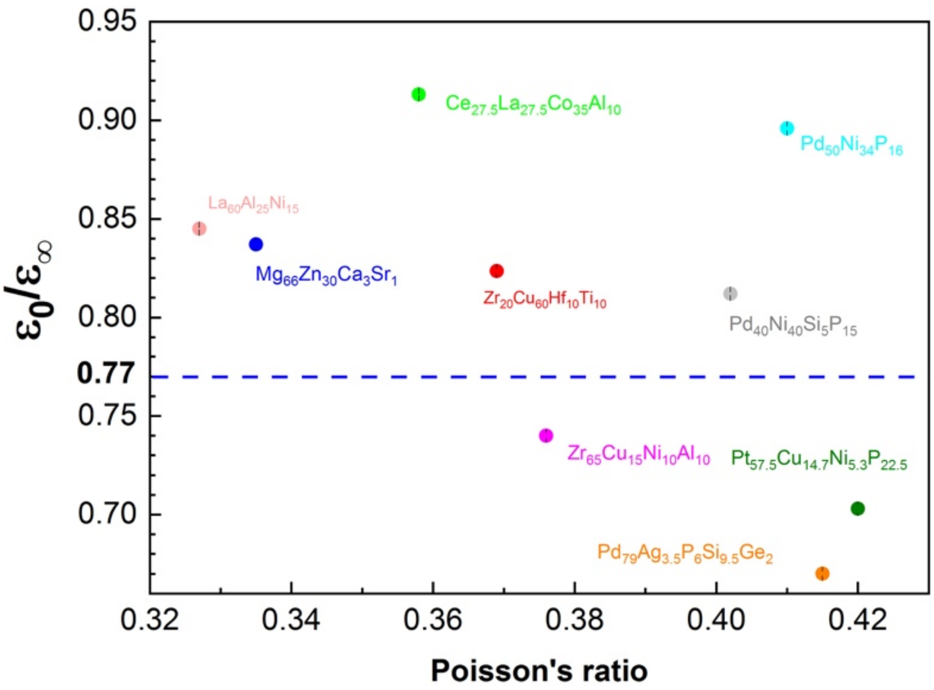

Figure 4.7 The strain ratio parameters with error bars of different BMGs with Poisson’s ratio larger than 0.32.

Among them, $La_{60}Al_{25}Ni_{15}$, $Mg_{66}Zn_{30}Ca_3Sr_1$, $Ce_{27.5}La_{27.5}Co_{35}Al_{10}$, $Cu_{60}Zr_{20}Hf_{10}Ti_{10}$ and $Pd_{50}Ni_{34}P_{16}$ are brittle according to the reported mechanical tests contrary to the conclusion drawn in [108]. Meanwhile, the brittle plastic behavior of these BMGs is manifested by their large strain ratio parameters that are above 0.77. The $Zr_{65}Cu_{17}Ni_8Al_{10}$, $Pt_{57.5}Cu_{14.7}Ni_{5.3}P_{22.5}$ and $Pd_{79}Ag_{3.5}P_6Si_{9.5}Ge_2$ with $\frac{\varepsilon_0}{\varepsilon_\infty}$ below 0.77 exhibit large plasticity. The plastic behavior of BMGs in Fig. 4.7 doesn't show increasing trend with the increase of ν. Fig. 4.7 shows that the correlation between the Poisson's ration and the plasticity of BMGs is weak. In contrast, it indicates that $\frac{\varepsilon_0}{\varepsilon_\infty}$ works much better to characterize the plasticity of various BMGs. Furthermore, according to Figs. 4.4 to 4.7, the presumption that BMGs with smaller $\frac{\varepsilon_0}{\varepsilon_\infty}$ shows more plasticity is firmly confirmed.

4.6 Characterization of the plasticity with the strain ratio parameter

The strain ration parameter in Figs. 4.4 to 4.7 is consistent with the plastic behavior of the measured BMGs. The correlation between the strain ratio parameter, $\frac{\varepsilon_0}{\varepsilon_\infty}$, and the plastic behavior of BMGs is well established. The "elastic" deformation is locally heterogenous and non-affine in BMGs [27]. When BMG is subjected to some stresses, the bond-cutting-and-reforming (BCR) [115, 116] will initiate to accommodate the deformation. Subsequently, the local strain is relaxed. This BCR behavior in the first shell of BMGs is known as the LTR. Therefore, the strain ratio parameter, $\frac{\varepsilon_0}{\varepsilon_\infty}$, measures the relaxed local strain and also quantifies the fraction of the activated LTRs. The LTRs are related to the nucleation of the emerging STZs that control the formation and propagation of the shear band in BMG during yielding. The independence of $\frac{\varepsilon_0}{\varepsilon_\infty}$ on external stress (Fig. 4.2) indicates that the fraction of LTR which can be activated is an intrinsic property of BMGs. If more LTRs can be activated, i.e. more STZs, the ability to accommodate the plastic deformation is higher. Thus, BMG with small $\frac{\varepsilon_0}{\varepsilon_\infty}$ is capable to bear more plastic deformation. As a result, the correlation of the microscopic deformation in elastic region, to the macroscopic plastic behavior of BMGs is well established using this parameter, $\frac{\varepsilon_0}{\varepsilon_\infty}$.

Based on the plastic behavior of various BMGs in Figs. 4.4 to 4.7, the critical value of $\frac{\varepsilon_0}{\varepsilon_\infty}$ is found to be 0.77. BMGs with $\frac{\varepsilon_0}{\varepsilon_\infty}$ below 0.77 tend to show large plasticity; while, with $\frac{\varepsilon_0}{\varepsilon_\infty}$ above 0.77, tend to show limited or little plasticity (Fig. 4.5 to Fig. 4.7). LTR is the only deformation defect of BMGs under elastic deformation to accommodate the local strain resulting in the local strain relaxation. Apparently, BMGs can bear more plastic deformation if more LTRs can be activated. The critical value of $\frac{\varepsilon_0}{\varepsilon_\infty}$, 0.77, indicates that BMGs exhibit ductile deformation behavior when more than 23% of the average strain can be relaxed locally which suggests the fraction of the activated LTRs is no less than 23%. This agrees well with the previous glass transition temperature theory [117] where the glass transition occurs when the fraction of the liquid-like spots reaches the percolation limit, 24.3%. When the activated LTRs reaches 23%, close to the percolation limit, the BMG exhibits the behavior where the percolation of STZ leads to the ease of multiple shear bands formation. In this way, the propagation of the dominant shear band is inhibited by other shear bands and BMG tends to present large plasticity. On the other hand, if the fraction of the STZ sites cannot reach the percolation limit, i.e. $\frac{\varepsilon_0}{\varepsilon_\infty}$ is above 0.77, BMG behaves with the brittle fracture where the dominant shear band propagates without any confinement. Through the simulation of the steady-state flow in the shear band, the failure resulting from the stress-induced glass transition at temperature below T_g was reported [118]. When $\frac{\varepsilon_0}{\varepsilon_\infty}$ is below 0.77, the imposed stress is distributed in the multiple shear bands which significantly relieves the stress localization. Consequently, to achieve the critical stress that induces the glass transition and formation of the dominant shear band, more external stresses need to be added and, thus, more plastic deformation is accommodated. The agreement of the critical value of $\frac{\varepsilon_0}{\varepsilon_\infty}$ with the percolation limit of the glass transition theory corroborates the physical meaning of the strain ratio parameter, $\frac{\varepsilon_0}{\varepsilon_\infty}$, and verifies the correlation of the microstructure to the plasticity of BMGs established by $\frac{\varepsilon_0}{\varepsilon_\infty}$.

4.7 Conclusions

Through the in-situ high-energy X-ray diffraction and the anisotropic PDF analysis, the local nonaffine deformation, or local topological rearrangement (LTR), activated by the stress exerted on BMGs is quantified experimentally for the first time by the proposed strain ratio parameter, $\frac{\varepsilon_0}{\varepsilon_\infty}$. The correlation of the microscopic deformation in elastic region, LTRs, to the macroscopic plastic behavior of BMGs is established. With this strain ratio parameter, $\frac{\varepsilon_0}{\varepsilon_\infty}$, the plastic behavior of BMGs can be predicted from their elastic deformation in a non-destructive way. BMGs with $\frac{\varepsilon_0}{\varepsilon_\infty}$ below the critical value, 0.77, tend to show more plasticity.

Chapter 5 Transformation pathway from alpha to omega and texture evolution in Zr via high-pressure torsion

5.1 Introduction

Zirconium is a refractory metal which is commonly used in nuclear and biomedical industries and is a main component of many bulk metallic glasses [22, 119, 120]. There are three known phases: α, β, and ω in zirconium, as shown in [88] (Fig. 2.11). The α phase, with a hexagonal closed packed (hcp) structure, is the stable phase under ambient conditions. It will transform to the ω phase (simple hexagonal) under pressure between ~2.3 - 6 GPa at room temperature (RT) or to the β phase (bcc structure) at high temperature of ~1100 K at 1 atm. At very high pressure, ~ 30 GPa, even at room temperature the ω phase will transform to β phase [89, 90, 91]. The ω phase is metastable at ambient conditions [121]. The microscopic mechanisms of thermodynamically driven transition between the α and β phases [90, 92, 94], and the martensitic transition between ω and β phase [93, 95] have been thoroughly described and are firmly established. However, there is still debate about the mechanism during the α to ω transformation. There are two principal pathways proposed for the α to ω transformation that originated in experimental studies of Ti and its alloys. The first model by Silcock [96] is a direct martensitic transformation from α to ω while the second suggested by Usikov and Zilbershtein [97] is an indirect mechanism through the intermediate β phase. Silcock proposed that the orientation relationship (OR) of the direct α to ω phase transition in Ti alloys is $(0002)_\alpha \parallel (11\bar{2}0)_\omega$, $[11\bar{2}0]_\alpha \parallel [0002]_\omega$. Based on a TEM study on samples of pure Zr in which, an $\alpha \rightarrow \omega$ transition was induced by high pressure, Rabinkin et al. [122] observed similar OR and proposed atomistic model of the direct α to ω phase transition in Zr (Fig. 5.1). Two stacking planes $(0002)_\alpha$ of the α phase are shown in Fig. 5.1 (a). The red circles

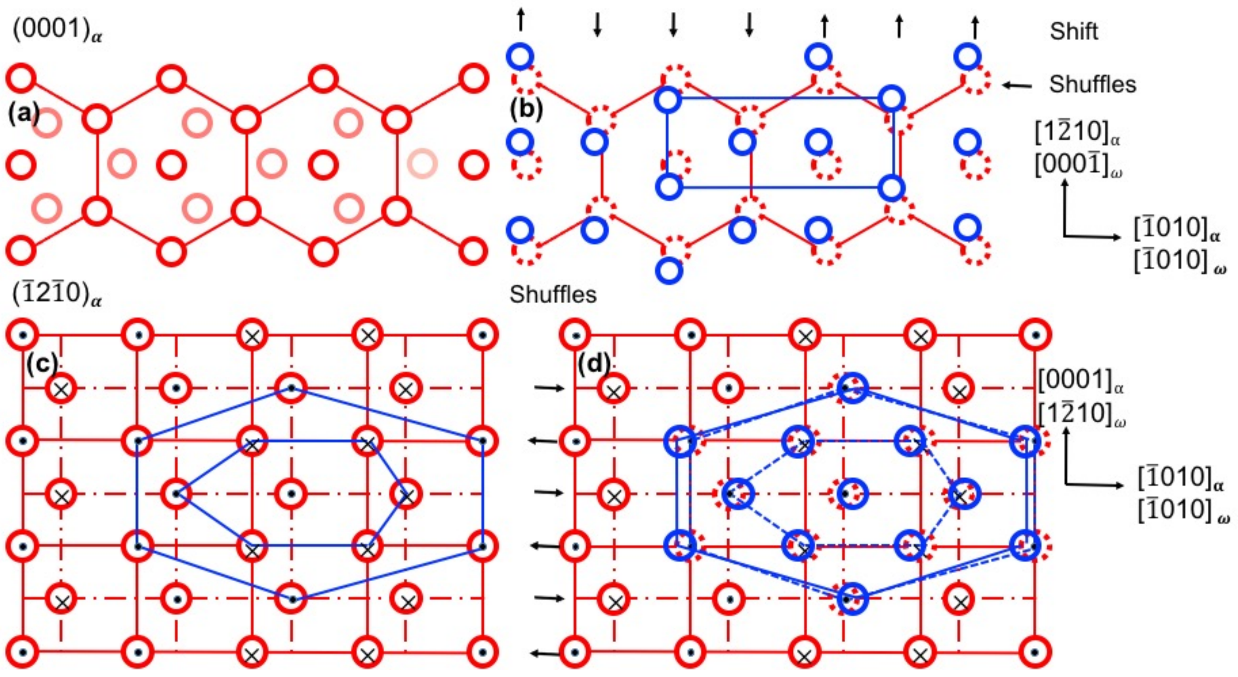

Figure 5.1 Atomistic model of direct α to ω phase transition in pure Zr proposed by Rabinkim et al. [120]. (a) This shows the two $(0002)_\alpha$ stacking planes of the α phase (the light red circles are the Zr atoms on the below $(0002)_\alpha$ plane). (b) After the shifts and shuffles, the blue circles are the displaced Zr atoms that formed the $(\bar{1}2\bar{1}0)_\omega$ plane from $(0002)_\alpha$ plane. (c) The $(\bar{1}2\bar{1}0)_\alpha$ plane of the α phase. The dot and cross in the atom shows the shuffle direction of it (outside or inside the paper). (d) The shuffle along the $[\bar{1}010]_\alpha$ direction forms a distorted $(0001)_\omega$ plane from $(\bar{1}2\bar{1}0)_\alpha$ plane.

are Zr atoms on the first $(0002)_\alpha$ plane and the light red circles are Zr atoms on the second plane below. The three out of six atomic rows along $[1\bar{2}10]_\alpha$ direction shift by 0.808 Å along the $[1\bar{2}10]_\alpha$ direction, as shown in Fig. 5.1 (b), while the other three atomic rows shift along the opposite direction. All the atoms on one $(0002)_\alpha$ plane shuffle by 0.233 Å along the $[\bar{1}010]_\alpha$ direction. Then the $(\bar{1}2\bar{1}0)_\omega$ plane is formed from the $(0002)_\alpha$ plane, as shown by the blue circles in Fig. 5.1 (b). This pathway corresponds to the first Silcock's condition $(0002)_\alpha \parallel (11\bar{2}0)_\omega$ and was recently observed in pressure studies in Zr [123] and by Adachi et al. [103] from high-pressure torsion (HPT). An indirect mechanism was suggested by Usikov and Zilbershtein [97] where the $\alpha \rightarrow \omega$ transformation proceeds as $\alpha \rightarrow \beta \rightarrow \omega$, i.e. through the intermediate β-phase, which is thermodynamically unstable in Ti and Zr at ambient conditions. The corresponding OR obtained through TEM studies was $(0002)_\alpha \parallel (01\bar{1}1)_\omega$, $[10\bar{1}0]_\alpha \parallel [\bar{2}\bar{1}31]_\omega$. Alternative pathway was also suggested for Ti by Trinkle et al. [98] from ab-initio calculations with OR $(0002)_\alpha \parallel (0\bar{1}11)_\omega$, $[11\bar{2}0]_\alpha \parallel [01\bar{1}1]_\omega$. There are other studies [99, 100, 101] on the pathway and OR of the α to ω phase transition in Zr and Ti, whereas no unanimous conclusion is drawn on this problem. Recently Perez-Prado and Zhilyaev [124] reported shear-induced transitions of α to both ω and β phases in the HPT experiment.

The shear induced α to ω phase transition under low pressure ~ 2.3 GPa in zirconium was first observed experimentally by Zilbershtein *et al.* [102] in 1975. Recently, there have been more reports on this transition by using the high-pressure-torsion (HPT) technique [89, 103, 104, 125]. In this technique, the sample is compressed, and torsion is applied under pressure.

During severe deformation in the HPT process, torsion texture is introduced to the zirconium sample. Furthermore, HPT can refine microstructure. For example, the nano-grained ω phase was fabricated after HPT [89]. Min Ma *et al.* have reported the textures of hot-rolled Zr and the cold rolled Zr [105]; however, the texture evolution due to HPT deformation has not been established. Recently Adachi et. al. [103] observed texture after HPT of Zr, by comparing two directions, which is insufficient to resolve full texture.

This section is focused on the phase transitions in pure Zr by HPT, examining crystallographic structures of the transformed phases through the X-ray profile refinement and texture. In particular, we examined the crystallographic orientation relationship of the α and ω phases and the possibility of $\alpha \rightarrow \beta \rightarrow \omega$ transformation. We determined texture evolution during HPT and phase fractions, clarified orientation relationships, and the microscopic pathway of the shear-induced α to ω phase transformation.

5.2 Experiment

High purity Zr metal rod (99.9%) was used in the experiment. However, since iodide purified Zr (van Arkel – de Boer process [126]) could be inhomogeneous due to low purity seed part, we re-melted Zr several times and cast into rod shape using the automatic arc melting and tilt-casting machine [127]. Thin discs with 10 mm in diameter and 1 mm in thickness were cut from Zr rods and processed by high-pressure torsion with constrained anvil geometry (Fig 5.2 (a)): with rotation of 0, 0.5, 1 and 5 turns (denoted as 0N, 0.5N, 1N and 5N) respectively under the compressive pressure of 5 GPa, as shown in Fig. 5.2 (a). Thin slabs with dimensions of $0.8 \times 0.8 \times 10$ mm^3 were cut along the diameter of the HPT-processed Zr plates (Fig. 5.2 (b)) by electrical discharge machining (EDM). Structural studies on the center and the edge parts of the slabs were carried out through synchrotron high-energy x-ray diffraction (100 keV, $\lambda = 0.1235$ Å) at the 1-ID and 6-ID beam lines of the Advanced Photon Source, Argonne National Laboratory. 2D detectors, placed ~120 cm behind the sample, with 2048 × 2048 pixels and 200μm × 200μm pixel size were used to

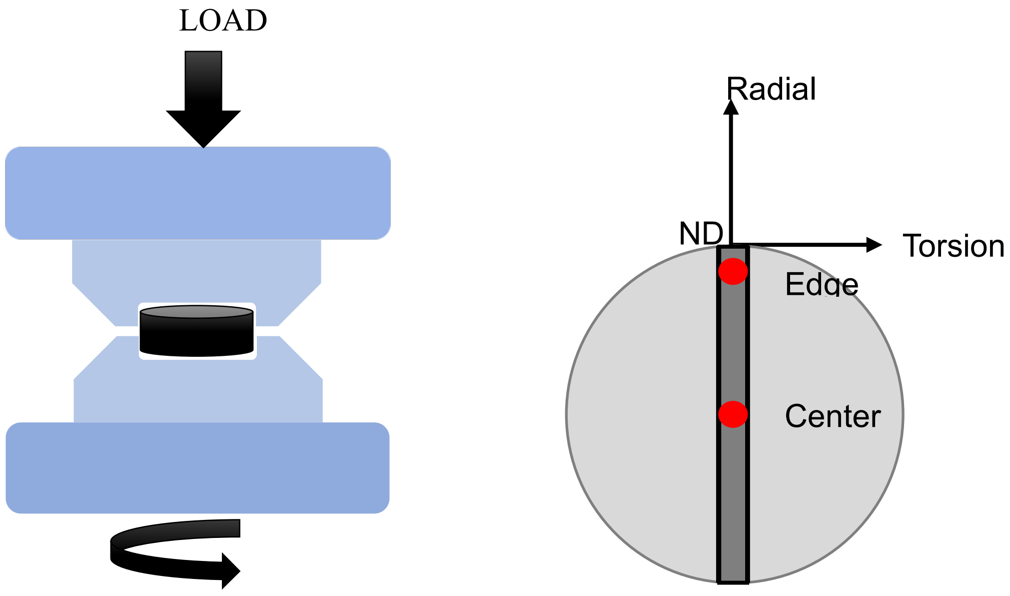

(a) (b)

Figure 5.2 Schematic diagram of (a) High Pressure Torsion process, (b) the orientation of the sample.

collect data at each beam line. Calibration was performed using the CeO_2 NIST powder standard. 2D diffraction data were processed by FIT2D software [110]. General structure analysis system (GSAS) [128], EXPGUI [129], and MAUD software [130] were used to fit the data and obtain the phase information.

To analyze texture, Zr slabs were mounted on the goniometer and high energy x-ray diffraction was collected using the 2D detector for the sample ϕ angle from 0° to 150° every 15° (Fig. 3.3). At $\phi = 0°$, Q_x is parallel to the torsion and Q_z || to the radial direction. At $\phi = 90°$, Q_x is parallel to the normal direction and Q_z || to the radial direction; $\mathbf{Q} = (Q_x,0,Q_z)$ defines the scattering vector in the plane of the sample, x-ray beam is along y direction. Diffraction patterns in the detector plane were binned in 72 5°-datasets. The texture and phase fractions were obtained by the Rietveld refinement in MAUD software [130] using 72 patterns for each sample orientation ϕ. Then, the MTEX [131] was used to recalculate the orientation distribution function (ODF) and the texture index (*TI*). The *TI* is the integral of the square of the texture function [132], $f(g)$.

$$\mathrm{TI} = \oint [f(g)]^2 dg \quad (1)$$

TI ranges from 1 to infinity. The large value of *TI* means strong texture.

5.3 Phase transition of HPT-Zr

5.3.1 Shear induced α to ω phase transition

Fig. 5.3 shows, as an example, the high-energy x-ray diffraction patterns from the edge part of the Zr samples: after compression of 5 GPa without torsion (left panel), and after high-pressure torsion under 5GPa for 5 rotations (right panel). The two-phase Rietveld refinement analysis including texture (described later in the paper) allowed us to determine the lattice parameters and the phase fractions with reasonable accuracy in each sample, as shown in Table 5.1 and Table 5.2.

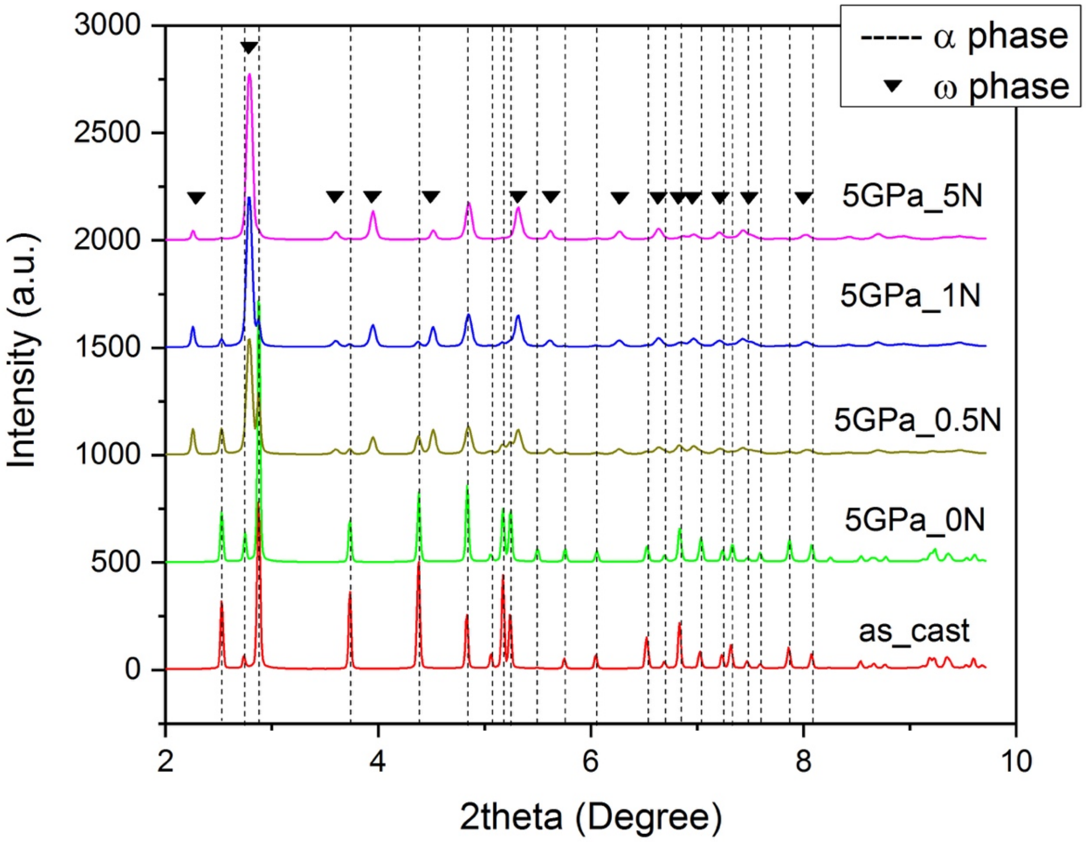

Figure 5.3 X-ray diffraction patterns from the edge part of the Zr samples (the red line is the as-cast Zr sample; the green line is the Zr sample under compression 5 GPa; the yellow line is the Zr sample under 5 GPa and 0.5 turn; the blue line is the Zr sample under 5 GPa and 1 turn; the pink line is the Zr sample under 5 GPa and 5 turns).

Table 5.1 Lattice parameters of Zr.

Zr samples	*α*-phase			*ω*-phase		
	a (Å)	c (Å)	c/a	a (Å)	c (Å)	c/a
0N	3.232	5.150	1.593	/	/	/
0.5N_Center	3.231	5.144	1.592	5.041	3.136	0.622
0.5N_Edge	3.231	5.146	1.593	5.040	3.131	0.621
1N_Center	3.230	5.147	1.593	5.039	3.132	0.622
1N_Edge	3.231	5.145	1.592	5.040	3.132	0.621
5N_Center	3.231	5.149	1.594	5.039	3.133	0.622
5N_Edge	3.230	5.146	1.593	5.040	3.132	0.621

Table 5.2 Phase fractions in Zr samples.

HPT-Zr	Center part		Edge part	
	α-phase fraction (%)	*ω*-phase fraction (%)	*α*-phase fraction (%)	*ω*-phase fraction (%)
Zr_0n	100	0	100	0
Zr_0.5n	87.88	12.12	21.07	78.93
Zr_1n	44.61	55.39	8.5	91.5
Zr_5n	20.7	79.3	5.34	94.66

In general, our results are consistent with previous finding that show ease of transition from alpha to omega under pressure with applied shear strain [e.g. 89, 103, 124, 102, 104, 125]. As the shear strain is larger, for example, at the edge of the sample or with increased number of rotations, the fraction of omega phase goes higher (see Table 5.2). The lattice parameters and *c/a* ratio for omega phase 0.622 ±0.002 are independent of the applied shear. The slightly higher than ideal *c/a* ratio is similar to values obtained under static pressure [88, 95, 133, 134] or by shock loading [135, 136]. The atomic volume is 23.29 Å^3 for alpha and 23.0 Å^3 for the omega phase. As shown in Fig. 5.3 and Table 5.2, the sample compressed at 5 GPa without torsion contain a single α phase. This implies that 5 GPa compressive pressure in our HPT machine is not sufficient to trigger the α to ω phase transition in Zr. From other studies, it appears that higher ratio of the shear to hydrostatic component induces transition at lower pressures [125, 137]. On the other hand studies performed in close to pure hydrostatic conditions suggest that transition occurs in the range from 5.5 to 6 GPa [95, 138]. Apparently, our constrained HPT setup has high quasi-hydrostatic component. However, application of shear strain on the compressed Zr by rotating the plunger by half turn results in the appearance of the ω phase. In general, the ease to trigger alpha→omega transition by a shear under pressure could be due to the negative pressure dependence of the shear modulus observed in hcp Zr [139, 140], which lowers resistance to shear driven transformation. In our data, with the increasing shear strain, the ω phase fraction increases from 0 (Zr_0N) to 94.66% (Zr_5N_Edge). The fraction of the α phase decreases to 5.34% (Zr_5N_Edge). Clearly the larger shear strain in the edge part favors the transition. Tables 5.1 and 5.2 quantitatively describe the effect of the shear strain on driving the transition from the α to ω.

Ideally, the geometrical center point would not undergo any deformation in the HPT process, however, in reality the center is ill defined during the torsion and also the x-ray beam probes fixed volume of the deformed sample [42, 80]. Therefore, for the purpose of further analysis we assume that higher fraction of ω phase corresponds to a larger effective shear strain.

5.3.2 Rejecting the formation of β phase during HPT process

Fig. 5.4 is a part of the high energy x-ray diffraction pattern of the 5GPa_5N sample covering range of 2theta from 6 to 8.5 degrees. Perez-Prado and Zhilyaev [124] claimed that they observed

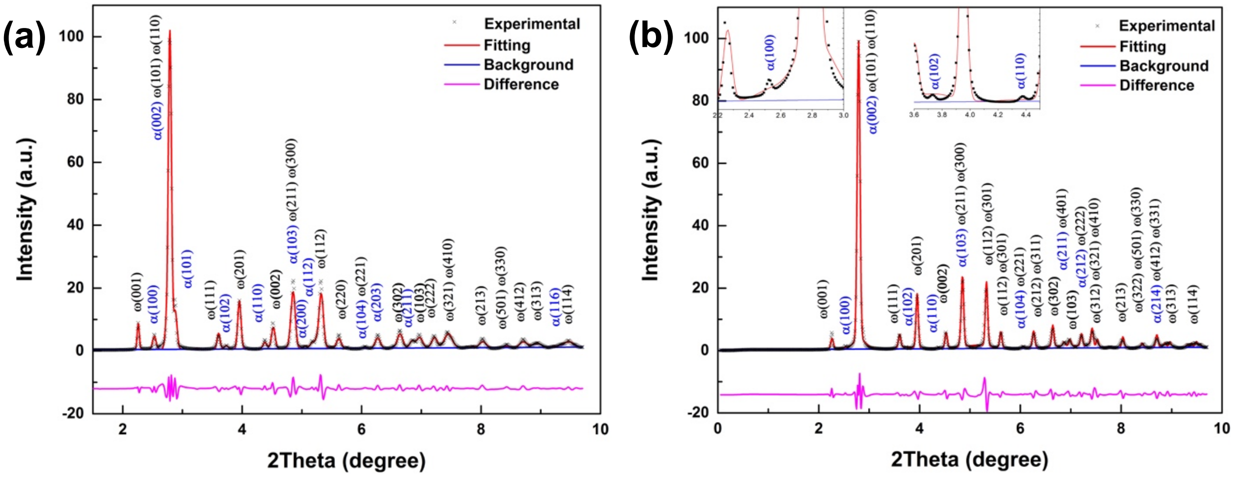

Figure 5.4 X-ray diffraction patterns of HPT-Zr under 5 GPa and 5 turns at (a) the center part and (b) the edge part of the sample.

the *α* to *β* phase transition in HPT-Zr and the *β* phase was stable at ambient condition. These conclusions were drawn based on the presence of a single *β* peak in the diffraction pattern (the second *β* peak that could be used to differentiate from the *ω* phase was absent in their data). In order to verify those findings in our study, we calculated the corresponding positions of the two *β* peaks they considered. These positions are marked by arrows in Fig. 5.5 at 6.86 and 7.96 degrees. In our high-resolution study, there is no peak at 7.96 degrees, and there is an *ω* peak at 8.1 degrees. Furthermore, the peak at 6.86 degrees (assigned to the *β* phase in [124]) is an overlap of $(211)_\alpha$ and $(401)_\omega$ peaks, and definitely, cannot be used to identify the *β* phase at all. Thus, there is no evidence that any fraction of the *β* phase (within resolution of the x-ray diffraction) is present as an outcome of the HPT process (at least) in our samples. Considering the general complexity of the *α*/*ω* diffraction pattern, we suggest that isolating beta peaks as a third phase is a rather problematic.

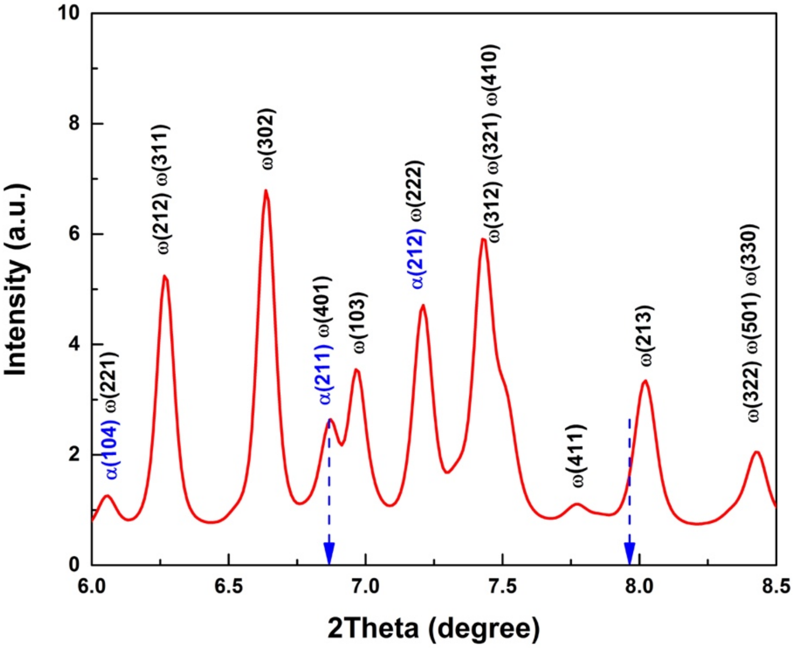

Figure 5.5 Part of the x-ray diffraction pattern of HPT-Zr under 5 GPa and 5 turns.

5.4 Transformation pathway of α to ω phase and texture evolution of HPT-Zr

The progress of texture with increasing shear strain is illustrated in Fig. 5.6. It shows the 2D diffraction patterns of Zr_0N, Zr_1N_edge, and Zr_5N_edge spots at the sample ϕ angle set at 0. For the Zr_0N sample, there are well separated diffraction spots, indicating that the grain size is large, in the order of ~200 micrometers, without any obvious texture. For the other HPT-processed samples, modulated rings are obtained, reflecting texture and grain size refinement during the process.

Based on the intensity variation of the Debye rings, ODFs are calculated in MAUD. Pole figures (PFs), that describe the orientation of the microstructure to the macroscopic sample processing directions, are used for representation (as shown in Fig. 5.7). Pole densities are expressed with the

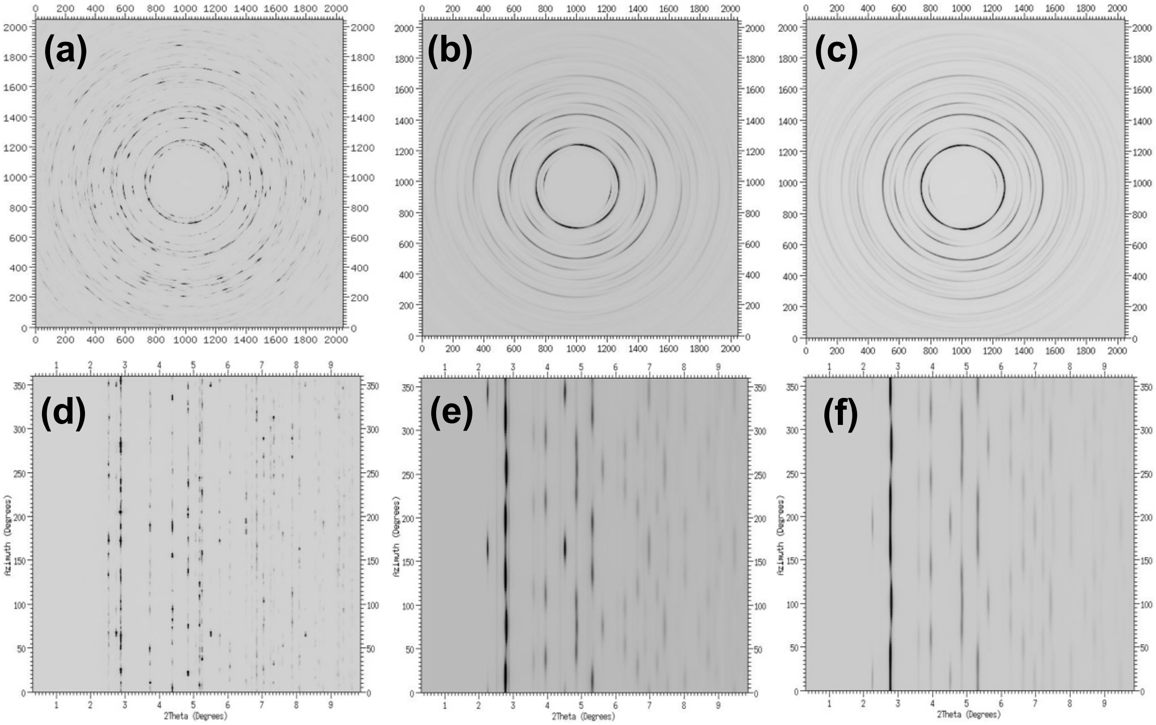

Figure 5.6 The 2D diffraction pattern and the Integrated pattern for different samples, (a) and (d) 0N sample; (b) and (e) 1N_Edge sample; (c) and (f) 5N_Edge sample.

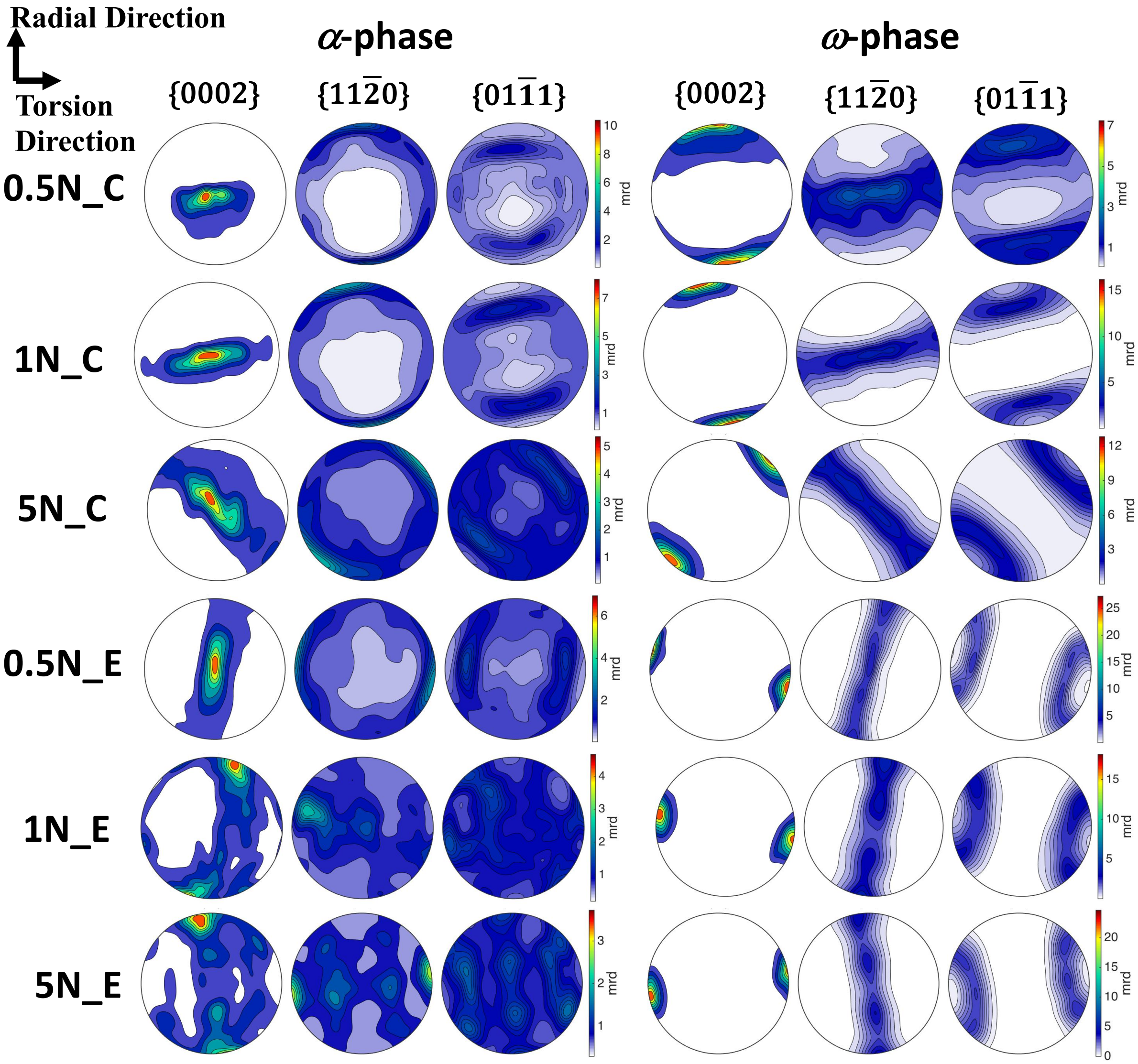

Figure 5.7 {0002}, {11$\bar{2}$0} and {01$\bar{1}$1} PFs of the α and ω phase of HPT-Zr samples.

multiple of the random distribution (mrd) in PFs. The definition of the orientation of the HPT-Zr samples is shown in Fig. 3.3: the radial direction is along the radius of the HPT disc, the torsion (shear strain) direction is along the tangent to the disc, and the normal direction is along the thickness of the disc.

The PFs of {0002}, $\{11\bar{2}0\}$ and $\{01\bar{1}1\}$ were investigated to explore the OR and distinguish competing transformation mechanism as shown in Fig. 5.7. The PF maps the crystallographic plane normals (in the reciprocal space) with respect to the sample orientation during diffraction. For 0.5N_C sample, the normal vector of the plane $\{0002\}_\alpha$ is in direction normal to the sample surface and $\{11\bar{2}0\}_\alpha$ is in the radial direction, respectively; correspondingly, the normal of the $\{0002\}_\omega$ is in the radial direction and normal of $\{11\bar{2}0\}_\omega$ is normal to the sample surface, respectively, These relations indicate the same directions of the $\{0002\}_\alpha$ and $\{11\bar{2}0\}_\omega$, and the $\{11\bar{2}0\}_\alpha$ and $\{0002\}_\omega$ and establish structural relationship between alpha and omega phases for this sample. Comparison of the PFs of all the HPT samples in Fig. 5.7 shows remarkable correlation between the PFs of $\{0002\}_\alpha$ and $\{11\bar{2}0\}_\omega$; $\{11\bar{2}0\}_\alpha$ and $\{0002\}_\omega$. This correlation persists even as the texture evolves during HPT and is maintained irrespective of phase fractions. This correlation clearly confirms direct martensitic transformation mechanism of α to ω with OR:

$$\{0002\}_\alpha // \{11\bar{2}0\}_\omega,$$

$$<11\bar{2}0>_\alpha // <0002>_\omega,$$

as proposed for Ti alloys by Silcock [96] and for Zr by Rabinkin [122].

Furthermore, from the symmetry of the hcp α phase, the ω phase can be formed by displacements along three independent $<11\bar{2}0>_\alpha$ directions resulting in formation of three variants of the ω phase [122]. These three variants are clearly seen in the pole figure for $\{11\bar{2}0\}_\omega$ when texture is strong, e.g. for the edge spots of the HPT samples. On the other hand, it can be also observed from Fig. 5.7 that the relationship $(0002)_\alpha \parallel (0\bar{1}11)_\omega$ expected for the transition through the intermediate beta phase does not hold at all thus contradicting that mechanism. This is the first time that full consistency with Silcock's OR is observed through texture analysis in the HPT induced transformation and microscopic mechanism [122] is confirmed.

There is no obvious texture in the as-cast sample and in the sample after compression only (Fig.5.6). However, texture quickly develops with applied torsion. The texture intensity of PFs of each phase (Fig. 5.7) indicates that both the α and ω phases have strong basal texture. The *TI* in Table 5.3 shows that the texture of the ω phase becomes stronger; while, interestingly, the texture of the α phase becomes weaker during the HPT process. With the increasing shear strain the $(0002)_\alpha$ plane, initially perpendicular to the normal direction, becomes perpendicular to the radial direction. For the ω phase, the $(0002)_\omega$ plane is normal to the radial direction when the ω phase begins to transform from the α phase, then is reoriented to the normal to the torsion direction. The comparison of the texture evolution of these two phases (Fig. 5.7) implies that the basal planes of the α and ω phases are always perpendicular to each other, $(0002)_\alpha \perp (0002)_\omega$. The schematic cartoon of texture evolution of both the α and ω phases are shown in Fig. 5.8. The red hexagonal

Table 5.3 Texture Index (TI) of HPT-Zr samples

HPT-Zr	Texture Index	
	alpha	omega
Zr_0.5n_center	3.22	2.33
Zr_1n_center	2.65	5.54
Zr_5n_center	1.85	4.66
Zr_0.5n_edge	1.36	9.94
Zr_1n_edge	1.46	7.67
Zr_5n_edge	1.36	9.26

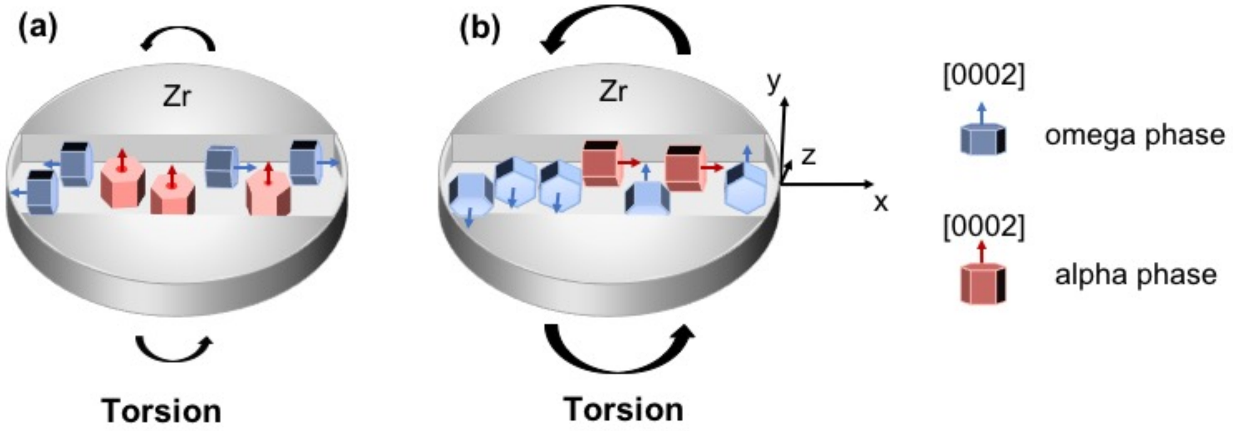

Figure 5.8 Schematic figure of the texture resolution for both α and ω phases. The orientation of the two phases of the sample with less shear strain (a), and with more shear strain (b). The red hexagonal prism is the hcp unit cell of the α-phase and the blue hexagonal prism is the simple hexagonal unit cell of the ω phase. The arrows on these hexagonal prisms show the [0002] direction. The x, y, and z axes are the radial direction, torsion direction, and the normal direction on the specific point respectively. Based on the right-hand rule, the z axes here is pointing outside.

prism is the unit cell of the α phase, and the blue hexagonal prism is the unit cell of the ω phase. The x, y, and z directions are the radial direction, torsion direction, and normal direction, respectively. It shows the relation $(0002)_{\alpha}\perp(0002)_{\omega}$ and the rotation of the *c*-axis for both phases during the HPT process.

It is reasonable to assume that the texture evolution of both the α and ω phases is controlled by the martensitic transformation and torsion (no texture in the as prepared and compressed only sample was observed). The strong basal texture of α of Zr_0.5N_Center sample (Fig. 5.7) is similar to that reported for rolled Zr [101] and HPT Ti [141]. Chen *et. al.* [141] studied the microstructure evolution of HPT Ti through electron backscattering diffraction (EBSD) and TEM. They found that $\{10\bar{1}2\}$ tensile twins appeared initially after compression and then torsion strain resulted in strong basal texture which is similar with the texture of Zr_0.5N_Center sample in this study. This strong basal texture is mainly caused by the activation of the basal slip system, {0001}<11$\bar{2}$0>, during shear deformation. The activation of the basal slip system of the Zr_0.5N_Center sample due to tensile twins formed during the compression stage is also verified through the comparison of experiment and simulation of Kanitpanyacharoen et. al. [142] for compressed Hf. The reorientation of the basal texture of the α phase to the radial direction with the increasing shear strain is caused by the prismatic slip, {10$\bar{1}$0}<11$\bar{2}$0>; where the prismatic slip overcomes the basal slip because tensile twins are becoming exhausted with increasing torsion, e.g. Sanchez *et. al.* [143]. The prismatic slip system, {10$\bar{1}$0}<11$\bar{2}$0>, is the primary slip system for hcp Zr. The texture of the α phase is becoming weaker since the *TI* decreases from 3.22 to 1.36 (Table 5.3). One would expect an increase in the *TI* of the α phase because torsion process should lead to enhanced texture. Clearly it is the transformation action that transforms preferentially oriented grains (c_α || normal direction) of α to ω effectively reducing the texture of α. As a result, both fraction and *TI* of the α phase become smaller.

Initially, when the α texture is strong and the fraction of α phase is high the texture of ω is determined by the transformation crystallographic OR. Thus, initial texture of ω is a result of a strong texture of α and the martensitic transformation proceeding accordingly to the $\{0002\}_\alpha$ // $\{11\bar{2}0\}_\omega$, $<11\bar{2}0>_\alpha$ // $<0002>_\omega$. With increasing torsion the basal texture of the ω phase becomes stronger (Table 5.3) and the texture component in $\{0002\}_\omega$ PF rotates from the radial to the torsion direction step by step (Fig. 5.7), indicating the torsion's dominant role in the further texture evolution of the ω phase. This is most likely due to the active {10$\bar{1}$0}[0002] slip system. Indeed, according to the simulation of Kumar *et. al.* [144], unlike the α-phase, the {10$\bar{1}$0}[0002] slip system is the primary slip system for the ω phase of Zr and Ti.

Chapter 6 Conclusions

From the engineering point of view, metallic glass is a unique and promising structural material which utilization is limited by the lack of RT plasticity. To understand this problem, the investigation of mechanical deformation and the deformation mechanism is essential. The elucidation of deformation mechanism of metallic glasses can also propel the understanding of the amorphous materials which are difficult to characterize. This work has addressed several critical questions related to the mechanical deformation of metallic glasses. To conclude, we summarize the main contributions of this work:

1. Through the in-situ high energy X-ray diffraction, the local nonaffine deformation, local strain relaxation, activated by the stresses exerted on BMGs is observed. When BMG is subjected to stresses below the yield strength, the local topological rearrangement mainly occurs in the first shell of BMG. To analyze the diffraction of the deformed glass structure, the anisotropic PDF analysis is used, then the *r*-dependent strains are obtained. Finally, the strain ratio parameter, the ratio of the local *r*-dependent strain to the long-range average strain, is proposed to quantify the local strain relaxation.
2. Through the measurement of the strain ratio parameter for various BMGs and the compression mechanical tests, it is verified that the strain ratio parameter is related to the plasticity of BMGs. Since the strain ratio parameter is a direct measure of the microstructure response to the external stimulus, the correlation of the microscopic deformation, the local strain relaxation, to the macroscopic plastic behavior of BMGs is established using this parameter, $\frac{\varepsilon_0}{\varepsilon_\infty}$.
3. A predictive way is found to characterize the plasticity of BMGs with the strain ratio parameter we proposed. The strain ratio parameter, $\frac{\varepsilon_0}{\varepsilon_\infty}$, can assess the plastic behavior of BMGs from their elastic deformation.

The α to ω phase transition of Zr has been studied for decades. However, still no unanimous conclusions are drawn. This work has addressed several critical questions related to the α to ω phase transition of Zr during HPT process. To conclude, we summarize the main accomplishments of this work:

4. Through the in-situ high energy X-ray diffraction, the $\alpha \rightarrow \omega$ phase transition of HPT-Zr is clarified and the formation of β phase is excluded. With the Rietveld refinement, the phase evolution and the phase fractions are revealed.
5. With the analysis of MAUD and MTEX, the texture of both α and ω phases of HPT-Zr at different shear strains is characterized by the pole figures. The mechanism of texture evolution of both alpha and omega is controlled by an OR during martensitic transformation and slip systems during torsion.
6. Based on the PFs, *TI*, and the phase fraction of each sample, we confirm the OR of the martensitic shear-induced α to ω phase transition in HPT-Zr. The ORs and phase analysis show that the α to ω phase transition is a direct phase transition consistent with the Silcock/Rabinkin transformation pathway without the formation of the intermediate β phase.

We also raised questions and research directions from a new perspective. Some outstanding possibilities are discussed below.

1. The characterization method, anisotropic PDF analysis, developed in present work can be expanded to other amorphous materials, especially oxide glasses and polymers. Oxide glass, e.g. fused silica, has well-defined coordination number, differing from metallic glasses. Amorphous polymers have the chain-like structure. How local stress is relaxed in such network structure and chain-like structure is not clear.

2. The anisotropic PDF analysis can also be expanded to study metallic glass composites. The deformation mechanism of these composites is different from BMG because of the second crystalline phase. The validity of the strain ratio parameter to characterize the plasticity of these material is not clear.
3. Further work is needed to understand why Zr-based BMGs with higher Zr content and $Pt_{57.5}Cu_{14.7}Ni_{5.3}P_{22.5}$ BMG have high tendency towards LTR, i.e. strain ratio parameter is below 0.77 based on the results in Chapter 4. If this can be solved, then the design of ductile metallic glasses is possible.

Reference

[1] W. L. Johnson, K. Samwer, Phys. Rev. Lett. 95 (2005) 195501.

[2] M. D. Demetriou, M. E. Launey, G. Garrett, J. P. Schramm, D. C. Hofmann, W. L. Johnson, R. O. Ritchie, Nat. Mater. 10 (2011) 123-128.

[3] A. Inoue, A. Takeuchi, Acta Mater. 59 (2011) 2243.

[4] W. Klement, R. Willens, P. Duwez, Nature 187 (1960) 869.

[5] A. L. Greer, Science 267 (1995) 1947.

[6] H. S. Chen, C. E. Miller, Rev. Sci. Instru. 41 (1970) 1237.

[7] H. S. Chen, Acta Metall. 22 (1974) 1505.

[8] H. W. Kui, A. L. Greer, D. Turnbull, Appl. Phys. Lett. 41 (1982) 716.

[9] A. Inoue, T. Nakamura, N. Nishiyama, T. Masumoto, Mater. Trans. JIM 33 (1992) 937.

[10] A. Inoue, T. Nakamura, T. Sugita, T. Zhang, and T. Masumoto, Mater. Trans. JIM 34 (1993) 351.

[11] J. Schroers, T. M. Hodges, G. Kumar, H. Raman, A. J. Barnes, Q. Pham, T. A. Waniuk, Mater. Today, 14 (2011) 1-2.

[12] https://www.liquidmetal.com/process/.

[13] A. Inoue, A. Takeuchi, Mater. Trans. JIM 43 (2002) 1892.

[14] A. Inoue, B. Shen, H. Koshiba, H. Kato, A.R. Yavari, Nat. Mater. 2 (2003) 661-663.

[15] S. J. Pang, T. Zhang, K. Asami, A. Inoue, Acta Mater. 50 (2002) 489-497.

[16] J. R. Scully, A. Gebert, J. H. Payer, J. Mater. Res. 22 (2007) 302-313.

[17] A. G. Perez-Bergquist, H. Bei, K. J. Leonard, Y. Zhang, S. J. Zinkle, Intermetallics 53 (2014) 62-66.

[18] H. U. Kunzi. Top Appl. Phys. 53 (1983) 169.

[19] S. Jovanovic, C. S. Smith, J. Appl. Phys. 32 (1961) 161.

[20] B. Golding, B. G. Bagley, F. S. L. Hsu, Phys. Rev. Lett. 29 (1972) 68.

[21] A. Inoue, Mater. Sci. Eng. A, 304-306 (2001) 1-10.

[22] T. Egami, T. Iwashita, W. Dmowski, Metals, 3 (2013) 77-113.

[23] T. Egami, D. Srolovitz, J. Phys. F, 12 (1982) 2141–2163.

[24] Y. Tong, W. Dmowski, H. Bei, Y. Yokoyama, T. Egami, Acta Mater. 148 (2018) 384-390.

[25] J. Brechtl, H. Wang, N.A.P.K. Kumar, T. Yang, Y.-R. Lin, H. Bei, J. Neuefeind, W. Dmowski, S.J. Zinkle, J. Nucl. Mater. 526 (2019) 151771.

[26] T. Egami, Prog. Mater. Sci. 56 (2011) 637–653

[27] W. Dmowski, T. Iwashita, C.-P. Chuang, J. Almer, and T. Egami. Phys. Rev. Lett. 105 (2010) 205502.

[28] C.A. Schuh, T.C. Hufnagel, U. Ramamurty, Acta Mater. 55 (2007) 4067-4109.

[29] D. Klaumunzer, R. Maaß, J.F. Loffler, J. Mater. Res. 26 (2011) 1453–1463.

[30] F. Shimizu, S. Ogata, J. Li, Acta Mater. 54 (2006) 4293–4298.

[31] V. K. Sethi, R. Gibala, A. H. Heuer, Scr. Metall. 12 (1978) 207.

[32] P. E. Donovan, W.M. Stobbs, Acta Metall. 29 (1981) 1419.

[33] E. Pekarskaya, C. P. Kim, W. L. Johnson, J. Mater. Res. 16 (2001) 2513.

[34] N. P. Bailey, J. Schiotz, K. W. Jacobsen. Phys. Rev. B 73 (2006) 064108.

[35] Q. Li, M. Li, Appl. Phys. Lett. 88 (20062) 41903.

[36] M. Wakeda, Y. Shibutani, S. Ogata, J. Park, Intermetallics 15 (2007) 139-144.

[37] Y.F. Shi, M.L. Falk, Acta Mater. 55 (2007) 4317-4324.

[38] J.J. Lewandowski, A.L. Greer, Nat. Mater. 5 (2006) 15-18.

[39] B. Yang, M.L. Morrison, P.K. Liaw, R.A. Buchanan, G.Y. Wang, C.T. Liu, M. Denda, App. Phys. Lett. 86 (2005) 141904.

[40] B. Yang, P.K. Liaw, G. Wang, M. Morrison, C.T. Liu, R.A. Buchanan, Y. Yokoyama, Intermetallics 12 (2004) 1265–1274.

[41] W. H. Jiang, M. Atzmon, Acta Mater. 51 (2003) 4095.

[42] J. Li, Z. L. Wang, T. C. Hufnagel, Phys. Rev. B 65 (2002) 144201.

[43] H. Chen, Y. He, G. J. Shiflet, S. J. Poon, Nature 367 (1994) 541.

[44] F. Spaepen, Acta Metall. 25 (1977) 9.

[45] A.S. Argon, Acta Metall. 27 (1979) 11.

[46] M.H. Cohen, D. Turnbull, J. Chem. Phys. 31 (1959) 1164.

[47] J.M. Ziman, Philos. Mag. 6 (1961) 1013.

[48] P. Murali, U. Ramamurty, Acta Mater. 53 (2005) 1467.

[49] Y. Yokoyama, T. Yamasaki, P.K. Liaw, A. Inoue, Acta Mater. 56 (2008) 6097.

[50] A. S. Argon, H. Y. Kuo, Plastic flow in a disordered bubble raft (an analog of a metallic glass). Mater. Sci. Eng. 39 (1979) 101-109.

[51] A. S. Argon, H. Y. Kuo, Free energy spectra for inelastic deformation of five metallic glass alloys. J. of Non-Cryst. Solids 37 (1980) 241-266.

[52] A. S. Argon, L. T. Shi, Development of visco-plastic deformation in metallic glasses. Acta Metall. 31 (1983) 499 – 507.

[53] Y. Fan, T. Iwashita, T. Egami, Nat. Commun. 5 (2014) 5083.

[54] I.C. Choi, Y. Zhao, Y.J. Kim, B.G. Yoo, J.Y. Suh, U. Ramamurty, J.I. Jang, Acta Mater. 60 (2012) 6862.

[55] L. Wang, Z.P. Lu, and T.G. Nieh. Scr. Mater. 65 (2011) 759–762.

[56] D. Pan, A. Inoue, T. Sakurai, M.W. Chen, PNAS 105 (2008) 39.

[57] Z.F. Zhang, J. Eckert, L. Schultz, Acta Mater. 51 (2003) 1167–1179.

[58] P.E. Donovan. Acta Mater. 37 (1989) 445.

[59] T. Mukai, T.G. Nieh, Y. Kawamura, A. Inoue, K. Higashi, Scr. Mater. 46 (2002) 43.

[60] W.J. Wright, R. Saha, W.D. Nix, Mater. Trans. JIM 42 (2001) 642.

[61] A. Inoue, W. Zhang, T. Zhang, K. Kurosaka, Acta Mater. 49 (2001) 2645.

[62] P. Lowhaphandu, S.L. Montgomery, J.J. Lewandowski, Scr. Mater. 41 (1999) 19.

[63] W. Johnson, MRS Bull. 24 (1999) 42.

[64] W. F. Wu, Y. Li, C. A. Schuh, Philos. Mag. 88 (2008) 71-89.

[65] A. T. Zehnder, Fracture mechanics, Springer Netherlands, 2012.

[66] W. Chen, J. Ketkaew, Z. Liu, R. M. O. Mota, K. O'Brien, C. S. Silva, J. Schroers, Scr. Mater. 107 (2015) 1–4.

[67] Y. Tong, W. Dmowski, Y. Yokoyama, G. Wang, P. Liaw, T. Egami, Scr. Mater. 69 (2013) 570–573.

[68] J. Schroers, W. L. Johnson, Phys. Rev. Lett. 93 (2004) 255506.

[69] Q. Wang, J. J. Liu, Y. F. Ye, T. T. Liu, S. Wang, C. T. Liu, J. Lu, Y. Yang, Mater. Today, 20 (2017) 293-300.

[70] L. Zhang, Y. Q. Cheng, A. J. Cao, J. Xu, E. Ma, Acta Mater. 57 (2009) 1154–1164.

[71] M. Kohda, O. Haruyama, T. Ohkubo, T. Egami, Phys. Rev. B 81 (2010) 092203.

[72] Y. Tong, T. Iwashita, W. Dmowski, H. Bei, Y. Yokoyama, T. Egami, Acta Mater. 86 (2015) 240-246.

[73] F. Faupel, W. Frank, M.-P. Macht, H. Mehrer, V. Naundorf, K. Rätzke, H. R. Schober, S. K. Sharma, H. Teichler, Rev. Mod. Phys. 75 (2003) 237.

[74] J. S. Langer, Phys. Rev. E 70 (2004) 041502.

[75] G. Kumar, P. Neibecker, Y. H. Liu, J. Schroers, Nat. commun. 4 (2013) 1536.

[76] L. Zhang, Y. Q. Cheng, A. J. Cao, J. Xu, E. Ma, Acta Mater. 57 (2009) 1154–1164.

[77] Y.H. Liu, G. Wang, R. J. Wang, D. Q. Zhao, Mi. X. Pan, W. H. Wang, Science 315 (2007) 1385-1388.

[78] A. Peker, W.L. Johnson, Appl. Phys. Lett. 63 (1993) 2342.

[79] Y. Zhang, W. H. Wang, A. L. Greer, Nat. Mater. 5 (2006) 857-860.

[80] W. Dmowski, Y. Yokoyama, A. Chuang, Y. Ren, M. Umemoto, K. Tsuchiya, A. Inoue, T. Egami, Acta Mater. 58 (2010) 429.

[81] S. V. Ketov, Y. H. Sun, S. Nachum, Z. Lu, A. Checchi, A. R. Beraldin, H. Y. Bai, W. H. Wang, D. V. Louzguine-Luzgin, M. A. Carpenter, A. L. Greer, Nature 524 (2015) 200–203.

[82] H. Guo, P. F. Yan, Y. B. Wang, J. Tan, Z. F. Zhang, M. L. Sui, E. Ma, Nat. Mater. 6 (2007) 735-739.

[83] D. Jang, J. R. Greer, Nat. Mater. 9 (2010) 215-219.

[84] Z. T. Wang, J. Pan, Y. Li, C. A. Schuh, Phys. Rev. Lett. 111 (2013) 135504.

[85] J. Pan, Y.X. Wang, Y. Li, Acta Mater. 136 (2017) 126-133.

[86] J. Pan, Y.X. Wang, Q. Guo, D. Zhang, A. L. Greer, Y. Li, Nat. Commun. 9 (2018) 560.

[87] H. Choi-Yim, R. Busch, U. Köster, W. L. Johnson, Acta Mater. 47 (1999) 2455.

[88] J. Zhang, Y. Zhao, C. Pantea, J. Qian, L.L. Daemen, P.A. Rigg, R.S. Hixson, C.W. Greeff, G.T. Gray, Y. Yang, and L. Wang, J. Phys. Chem. Solids. 66 (2005) 1213-1219.

[89] M.T. Pérez-Prado, A.A. Gimazov, O.A. Ruano, M.E. Kassner, A.P. Zhilyaev, Scr. Mater. 58 (2008) 219-222.

[90] W.G. Burgers, Physica. 1 (1934) 561-586.

[91] H. Xia, S. J. Duclos, A. L. Ruoff, Y. K. Vohra, *Phys. Rev. Lett.* 64 (1990) 204-207.

[92] F. Willaime, C. Massobrio, Phys. Rev. Lett. 63 (1989) 2244-2247.

[93] S.K. Sikka, Y.K. Vohra, R. Chidambaram, Prog. Mater. Sci. 27 (1982) 245-310.

[94] Y. K. Vohra, S. K. Sikka, R. Chidambaram, Bull. Mater. Sci. 3 (1981) 109-117.

[95] D.R. Trinkle (2003). A theoretical study of the HCP to omega martensitic phase transition in Titanium (Doctoral Dissertation). The Ohio State University, Columbia, Ohio.

[96] J.M. Silcock, Acta Metall. 6 (1958) 481-493.

[97] M.P. Usikov, V.A. Zilbershtein, Phys. Stat. sol. (A) 19 (1973) 53-58.

[98] D.R. Trinkle, R.G. Hennig, S.G. Srinivasan, D.M. Hatch, M.D. Jones, H.T. Stokes, R.C. Albers, J. W. Wilkins, Phys. Rev. Lett. 91 (2003) 025701.

[99] P.S. Ghosh, A. Arya, R. Tewari, G. K. Dey, J. Alloy. Compd. 586 (2014) 693-698.

[100] G. Jyoti, K.D. Joshi, S.C. Gupta, S.K. Sikka, Philos. Mag. Let. 75 (1997) 291-300.

[101] N.A. Zarkevich, D.D. Johnson, Phys. Rev. B 93 (2016) 020104(R).

[102] V.A. Zilbershtein, N.P. Chistotina, A.A. Zharov, N.S. Grishina, E.I. Estrin, Fiz. Metal. Metalloved. 39 (1975) 445-447.

[103] N. Adachi, Y. Todaka, H. Suzuki, M. Umemoto, Scr. Mater. 98 (2015) 1-4.

[104] A.P. Zhilyaev, F. Gálvez, A. Sharafutdinov, M.T. Pérez-Prado, Mater. Sci. Eng. A. 527 (2010) 3918-3928.

[105] M. Ma, M. Li, Y. Tan, H. Yuan, W. Liu, Int. J. Miner. Metall. Mater. 21 (2014) 785-795.

[106] Takeshi Egami, Simon J.L. Billinge. Underneath the Bragg peaks. 2003

[107] L. Krämer, K. S. Kormout, D. Setman, Y. Champion, R. Pippan, Metals 5 (2015) 720-729.

[108] S.V. Madge, D.V. Louzguine-Luzgin, J.J. Lewandowski, A.L. Greer, Acta Mater. 60 (2012) 4800–4809.

[109] J. Ketkaew, W. Chen, H. Wang, A. Datye, M. Fan, G. Pereira, U. D. Schwarz, Z. Liu, R. Yamada, W. Dmowski, M. D. Shattuck, C. S. O’Hern, T. Egami, E. Bouchbinder, Jan Schroers, Nat. Commun. 9 (2018) 3271.

[110] A.P. Hammersley, S.O. Svensson, A. Thompson, H. Graafsma, A. Kvick, J.P. Moy, Rev. Sci. Instr. (SRI-94) 66 (1995) 2729-2733.

[111] T. Egami, Y. Tong, W. Dmowski, Metals 6 (2016) 22.

[112] Z. Bian, G.L. Chen, G. He, X.D. Hui, Mater. Sci. Eng. A 316 (2001) 135-144.

[113] C. Fan, C. Li, A. Inoue, Phys. Rev. B 61 (2000) 3761.

[114] Y. Yokoyama, K. Fujita, A.R. Yavari, A. Inoue, Philos. Mag. Lett. 89 (2009) 322-334.

[115] Y. Suzuki, J. Haimovich, T. Egami, Phys. Rev. B 35 (1987) 2162.

[116] W. Dmowski, Y. Tong, T. Iwashita, Y. Yokoyama, T. Egami, Phys. Rev. B 91 (2015) 060101.

[117] T. Egami, S.J. Poon, Z. Zhang, V. Keppens, Phys. Rev. B 76 (2007) 024203.

[118] P. Guan, M. Chen, T. Egami, Phys. Rev. Lett. 104 (2010) 205701.

[119] R. Tewari, D. Srivastava, G.K. Dey, J.K. Chakravarty, S. Banerjee, J. Nucl. Mater. 383 (2008) 153-171.

[120] L. Saldaña, A. Méndez-Vilas, L. Jiang, M. Multigner, J.L. González-Carrasco, M.T. Pérez-Prado, M.L. González-Martín, L. Munuera, N. Vilaboa, Biomaterials. 28 (2007) 4343-4354.

[121] K. Edalati, Z. Horita, S. Yagi, E. Matsubara, Mater. Sci. Eng. A 523 (2009) 277-281.

[122] A. Rabinkin, M. Talianker, O. Botstein, Acta Metall. 29 (1981) 691-698.

[123] H. R. Wenk, P. Kaercher, W. Kanitpanyacharoen, E. Zepeda-Alarcon, Y Wang, Phys. Rev. Lett. 111(2013) 195701.

[124] M.T. Pérez-Prado, A.P. Zhilyaev, Phys. Rev. Lett. 102 (2009) 4-7.

[125] B. Srinivasarao, A.P. Zhilyaev, M.T. Pérez-Prado, Scr. Mater. 65 (2011) 241-244.

[126] A. E. van Arkel, J. H. de Boer, Z. Anorg. Allg. Chem. 148 (1925) 345–350.

[127] Y. Yokoyama, Metall. Mater. Trans. B 46 (2015) 893-905.

[128] A.C. Larson, R.B. Von Dreele, Los Alamos Lab. Rep. LAUR 86-748 (2000).

[129] B.H. Toby, J. Appl. Cryst. 34 (2001) 210-213.

[130] I. Lonardelli, H.-R. Wenk, L. Lutterotti, M. Goodwin, J. Synchrotron Rad. 12 (2005) 354-360.

[131] F. Bachmann, R. Hielscher, H. Schaeben, Solid State Phenomena 160 (2010) 63-68.

[132] H.J. Bunge, Texture analysis in materials science: mathematical methods. London: Butterworth; 1982.

[133] J.C. Jamieson, Science 140 (1963) 72-73.

[134] A. Jayaraman, W. Klement, G.C. Kennedy, Phys. Rev. 131 (1963) 644-649.

[135] Y.K. Vohra, J. Nucl. Mater 75(1978), 288-293.

[136] D.W. Brown, J.D. Almer, L. Balogh, E.K. Cerreta, B. Clausen, J.P. Escobedo-Diaz, T.A. Sisneros, P.L. Mosbrucker, E.F. Tulk, S.C. Vogel, Acta Mater. 67 (2014), 383-394.

[137] A.P. Zhilyaev, I. Sabirov, G. Gonzalez-Doncel, J. Molina-Aldareguia, B. Srinvasarao, and M.T. Perez-Prado, Mater. Sci. Eng. A 528 (2011) 3496.

[138] J. Zhang, Y. Zhao, R.S. Hixson, G.T. Gray, L. Wang, W. Utsumi, S. Hiroyuki, and H. Takanori, Phys. Rev. B 78 (2008) 054119.

[139] E. S. Fisher, J. Appl. Phys. 41(1970) 2991-2998.

[140] W. Liu, B. Li, L. Wang, J. Zhang, and Y. Zhao, J. Appl. Phys. 104 (2018) 076102.

[141] Y. J. Chen, Y.J. Li, J. C. Walmsley, N. Gao, H. J. Roven, M. J. Starink, T. G. Langdon, J. Mater. Sci. 47 (2012) 4838–4844.

[142] W. Kanitpanyacharoen, S. Merkel, L. Miyag, P. Kaercher, C.N. Tome, Y. Wang, H.-R. Wenk, Acta Mater. 60(2012) 430-442.

[143] P. Sanchez, A. Pochettino, T. Chauveau, and B. Bacroix, J. Nucl. Mater. 298 (2001) 329-339.

[144] A. Kumar, C. A. Bronkhorst, and T. Lookman, J. Appl. Phys. 123 (2018) 045903.

Vita

Hui Wang was born in Shanxi Province, China. She graduated from Harbin Institute of Technology for Bachelor of Science and Master of Science degrees in Materials Science and Engineering in 2011 and 2013. She became a graduate student in Materials Science and Engineering at University of Tennessee-Knoxville in August 2013.